

Revealing altermagnetic Fermi surfaces with two Kondo impurities

Qiong Qin,¹ Toshihiro Sato,^{2,3} Marcin Raczkowski ,⁴ Jeroen van den Brink,^{2,3} Congjun Wu,^{1,5,6,7,*} and Fakher F. Assaad ,^{4,3,†}

¹*New Cornerstone Science Laboratory, Department of Physics, School of Science, Westlake University, Hangzhou 310024, Zhejiang, China*

²*Institute for Theoretical Solid State Physics, IFW Dresden, 01069 Dresden, Germany*

³*Würzburg-Dresden Cluster of Excellence ct.qmat, Germany*

⁴*Institut für Theoretische Physik und Astrophysik, Universität Würzburg, 97074 Würzburg, Germany*

⁵*Institute for Theoretical Sciences, Westlake University, Hangzhou 310024, Zhejiang, China*

⁶*Key Laboratory for Quantum Materials of Zhejiang Province, School of Science, Westlake University, Hangzhou 310024, Zhejiang, China*

⁷*Institute of Natural Sciences, Westlake Institute for Advanced Study, Hangzhou 310024, Zhejiang, China*

Motivated by recent advances in the study of altermagnetism, or unconventional magnetism, and in the realization and manipulation of two-impurity Kondo physics in real materials, we propose a phase-sensitive method to explore unconventional magnetic symmetries. Our method can be implemented with spin-resolved scanning tunneling microscopy to study two-impurity Kondo phenomena on altermagnetic metals by varying the distance and orientation between magnetic impurities. Using quantum Monte Carlo simulations, we analyze the spin splitting of the Kondo resonance, whose spatial distribution sensitively captures the symmetry of the underlying altermagnetic order. Furthermore, the impurity spin correlations reflects the anisotropy of the RKKY interaction due to the altermagnetic Fermi surface splitting. This work provides a framework for studying the competition between the Kondo effect, the RKKY interaction and altermagnetism, in the simplest possible system.

Introduction.— Unconventional magnetism (UM) [1, 2] was proposed based on Fermi surface instability in analogy to unconventional superconductivity two decades ago. It has recently attracted extensive attention [3–35], driven by experimental realizations and its potential applications in spintronics—particularly due to its absence of stray magnetic fields and suitability for terahertz (THz) high-frequency operations. Most existing studies have focused on its origin, classification, and interplay with superconductivity. However, its interaction with other quantum phenomena, such as Kondo physics, remains largely unexplored [36–38]. This raises a compelling question: could novel and intriguing physics emerge from the interplay between Kondo effects and unconventional magnetism?

To detect unconventional magnetism – particularly altermagnetism (AM) – transport measurements and spin-resolved angle-resolved photoemission spectroscopy (ARPES) have been extensively employed. In the case of ARPES [6, 10, 11, 13, 26–28], the identification primarily relies on observing spin splitting in single-particle spectra and comparing the experimental Fermi surfaces with those predicted by Density functional theory (DFT) calculations. Additionally, signatures such as the anomalous Hall effect and other transport phenomena [28] have been used as indirect evidence for the presence of AM. As in the theory of superconductivity, *smoking gun* experiments are phase-sensitive and directly probe the relative phase of an order parameter [39]. Our motivation is to propose a scanning-tunneling-microscopy (STM) experiment in the realm of Kondo physics with a spin polarized

tip [40].

Motivated by the above questions and experimental needs, we propose a phase-sensitive approach based on Kondo physics to detect AM (a form of unconventional collinear magnetism). Specifically, we incorporate an AM term into the conduction electron sector of the two-impurity Kondo model [41–49], as schematically illustrated in Fig. 1, and perform unbiased finite-temperature quantum Monte Carlo (FTQMC) simulations [50–52]. Our results show that Kondo resonance can sensitively reflect the underlying symmetry of the AM order, clearly distinguishing between two AM states of $d_{x^2-y^2}$ and d_{xy} symmetries. These symmetry features are also manifested in the spin-spin correlation functions mediated by the RKKY interaction. Moreover, we observe a crossover

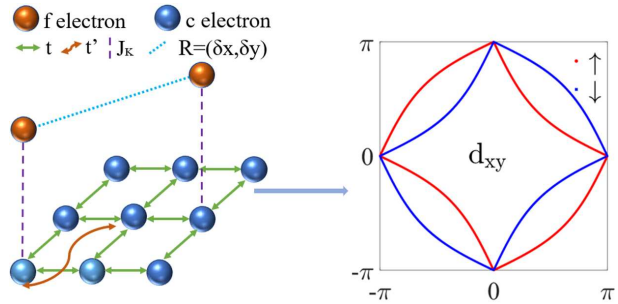


FIG. 1. Illustration of the two-impurity Kondo model, with the right panel depicting the Fermi surface of the underlying AM metal with $t' = 0.4$.

between the two-impurity and single-impurity regimes as the inter-impurity distance varies. The temperature-dependence analysis further reveals the competition between the RKKY interaction, Kondo effect and AM. Based on these findings, we propose that spin-resolved (SR)-STM measurements on magnetic impurities embedded in an AM metal can serve as a powerful phase-sensitive probe for detecting AM.

Model and method.— We consider the two-impurity Kondo model Hamiltonian with the conduction electrons exhibiting the *d*-wave-type AM band structure,

$$H = \sum_{\mathbf{k}\sigma} \epsilon_{\mathbf{k}\sigma} \hat{c}_{\mathbf{k}\sigma}^\dagger \hat{c}_{\mathbf{k}\sigma} + J_K \sum_{j=1,2} \hat{\mathbf{S}}_j \cdot \hat{\mathbf{s}}_j. \quad (1)$$

J_K describes the on-site antiferromagnetic Kondo coupling between localized magnetic impurities and conduction electrons with $\hat{\mathbf{S}}_j$ representing the impurity spin with $s = \frac{1}{2}$ at site j ; $\hat{\mathbf{s}}_j$ is the spin operator of conduction electrons on site j , which is defined as $\hat{\mathbf{s}}_j = \sum_{\alpha\beta} \hat{c}_{j\alpha}^\dagger \frac{\sigma_{\alpha\beta}}{2} \hat{c}_{j\beta}$ and $\hat{c}_{j\sigma}^\dagger$ creates a conduction electron at site j with the *z*-component of spin σ . The dispersion relation is given by: $\epsilon_{\mathbf{k}\sigma} = -2t[\cos k_x + \cos k_y] - 2t' \text{sgn}(\sigma)[\cos(k_x + k_y) - \cos(k_x - k_y)]$. t denotes the nearest-neighbor hopping and is set to unity below and t' is a next-nearest-neighbor hopping, yielding the d_{xy} -type spin splitting. Here, $\hat{c}_{\mathbf{k}\sigma}^\dagger$ creates a conduction electron in Bloch state \mathbf{k} and *z*-component of spin σ .

In the absence of impurities, the Bloch Hamiltonian possesses the spin group symmetry R_{sg} , *i.e.*, the spatial rotation at $\frac{\pi}{2}$ followed by the spin rotation at π flipping the *z*-component of spin, the C_{2v} with mirror planes along the diagonal directions. We will also study the two-impurity Kondo problem with $d_{x^2-y^2}$ -type AM band structure. In this case, the dispersion relation reads: $\epsilon'_{\mathbf{k}\sigma} = -2t[\cos k_x + \cos k_y] - 2t' \text{sgn}(\sigma)[\cos 2k_x - \cos 2k_y]$. The $d_{x^2-y^2}$ Hamiltonian has the same symmetry as the d_{xy} provided that the mirror reflection planes of the C_{2v} operations are along the *x* or *y* direction.

For the finite temperature auxiliary-field determinant QMC simulations, we adopt an Abrikosov fermion representation of the impurity spin [53] as, $\hat{\mathbf{S}}_j = \sum_{\alpha\beta} \hat{f}_{j\alpha}^\dagger \frac{\sigma_{\alpha\beta}}{2} \hat{f}_{j\beta}$, subject to the single-occupancy constraint $\sum_{\sigma} \hat{f}_{j\sigma}^\dagger \hat{f}_{j\sigma} = 1$ for $j = 1, 2$. The model enjoys the combined time-reversal (TR) and particle-hole symmetry as defined by $\hat{c}_{j\sigma}^\dagger \rightarrow \sum_s i\sigma_{\sigma,s}^y e^{i\mathbf{Q}\cdot\mathbf{j}} \hat{c}_{js}$ with $\mathbf{Q} = (\pi, \pi)$. This symmetry property of the Hamiltonian allows for a negative sign free FTQMC formulation of the model of Eq. (1) for both AM symmetries [54, 55]. Our implementation follows Refs. [56, 57] and we have used the Algorithms for Lattice Fermions (ALF) [58] implementation of the FTQMC. The lattice size is taken as $L = 12$ for the simulations.

Numerical results.— To at best understand how the AM band impacts the Kondo effect, it is convenient to formulate the action in terms of impurity spin $\mathbf{n}_i(\tau)$ and

fermion $\mathbf{c}_i^\dagger(\tau)$ coherent states. One can then integrate out the fermionic degrees of freedom that do not couple to the impurity spin so as to obtain the action:

$$S = S_0 + J_K \sum_{i=1}^2 \int_0^\beta d\tau s \mathbf{n}_i(\tau) \cdot \mathbf{c}_i^\dagger(\tau) \left(\frac{\sigma}{2}\right) \mathbf{c}_i(\tau) \quad (2)$$

$$+ \int_0^\beta \int_0^\beta d\tau d\tau' \sum_{i,j=1}^2 \mathbf{c}_i^\dagger(\tau) \mathbf{G}_0^{-1}(\tau - \tau', i - j) \mathbf{c}_j(\tau'),$$

where $[\mathbf{G}_0(\tau - \tau', i - j')]_{\sigma,\sigma'} = \langle T_\tau \hat{c}_{j,\sigma'}^\dagger(\tau') \hat{c}_{i,\sigma}(\tau) \rangle_0$ is the conduction electron Green function between the impurity sites in the absence of the Kondo coupling, and S_0 is the Berry phase of the spin-1/2 degrees of freedom, $s \mathbf{n}_i(\tau)$ with \mathbf{n}_i the unit vector on the S^2 sphere. The AM symmetries of the band are encoded in the spin dependence of the single particle Green function. As shown in the End Matter, if the displacement vector $\mathbf{R} = (\delta x, \delta y)$ between sites 1 and 2 is parallel to the nodal line in momentum space, then the Green function shows no spin dependence: It is proportional to the unit matrix in spin space. As a consequence, for this special orientation $SU(2)$ spin symmetry is restored and we expect no spin splitting of the Kondo resonance. This equally implies that single impurity problems with or without the AM term are symmetry equivalent. If the two impurities are not on a nodal line, then the Green function will acquire a spin dependence and we will see that this leads to a spin splitting of the Kondo resonance.

To capture the Kondo resonance in the realm of the Kondo model, we consider the composite fermion operator: $\hat{\psi}_{j\alpha}^\dagger = (\hat{c}_{j\alpha}^\dagger \sigma)_\alpha \cdot \hat{\mathbf{S}}_j$ [59–61]. This quantity transforms as the electron creation operator and the associated imaginary-time Green function is defined as, $\tilde{G}_{j\sigma}(\tau) = \langle T_\tau \hat{\psi}_{j\sigma}(\tau) \hat{\psi}_{j\sigma}^\dagger(0) \rangle$. The spin-resolved and frequency-dependent spectral function $\tilde{N}_\sigma(\omega)$ is obtained using the maximum entropy method via the spectral decomposition at $\tau > 0$, [62]:

$$\tilde{G}_{j,\sigma}(\tau) = \int d\omega \frac{\tilde{N}_{j,\sigma}(\omega) e^{-\omega\tau}}{e^{-\beta\omega} + 1}. \quad (3)$$

In Fig. 2 (a) and (b), the Green function $\tilde{G}_{\mathbf{R},\sigma}(\tau)$ and the corresponding spectral function $\tilde{N}_{\mathbf{R},\sigma}(\omega)$ exhibit a clear spin-dependent asymmetry in the presence of *d*-wave AM splitting, *i.e.*, $t' \neq 0$. When $t' = 0$, $\tilde{N}_{\mathbf{R},\sigma}(\omega)$ is spin-degenerate. At finite values of t' , the peak asymmetries with respect to $\pm\omega$ become spin-dependent, and are opposite for $\tilde{N}_{\mathbf{R},\uparrow}(\omega)$ and $\tilde{N}_{\mathbf{R},\downarrow}(\omega)$, respectively.

The spin-dependence of the asymmetry in $\tilde{N}_{\mathbf{R},\sigma}(\omega)$ relies on the orientation of the displacement vector \mathbf{R} . It becomes strongest when \mathbf{R} is along the anti-nodal directions, say, $(1, 1)$, for the d_{xy} type of AM. If \mathbf{R} is rotated by $\frac{\pi}{2}$, the spin-dependence is reversed, consistent with the spin-group symmetry R_{sg} . When \mathbf{R} is along the nodal

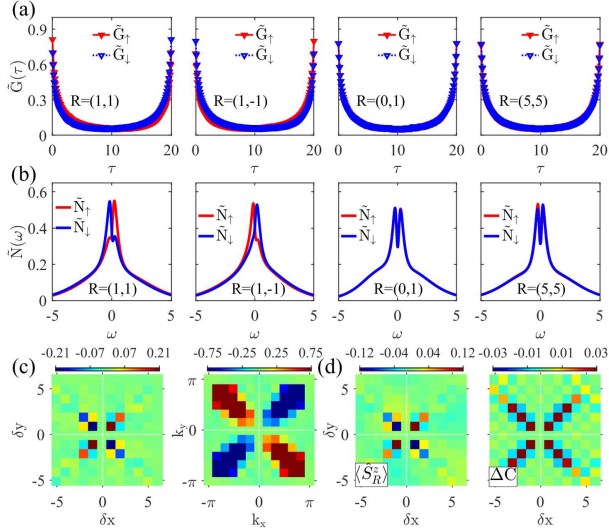


FIG. 2. d_{xy} AM symmetry at $J_K = 2$ and $t' = 0.4$. (a) Imaginary-time Green function of the composite fermion, $\tilde{G}_R(\tau)$, for varying impurity separations $\mathbf{R} = (\delta x, \delta y)$, where \mathbf{R} denotes the distance between the two magnetic impurities. (b) Corresponding spectral function $\tilde{N}_R(\omega)$ for different \mathbf{R} . (c) Real-space distribution of the difference $\Delta\tilde{G}_R$ between spin-up and spin-down Green functions, together with its Fourier transform. (d) Local magnetic moment $\langle \hat{S}_R^z \rangle$ and the real-space equal-time spin correlation functions between the two impurities, showing the anisotropy $\Delta C_R = C_R^x(0^+) - C_R^z(0^+)$. Temperatures are $T = 0.05$ for (a)(b), and $T = 0.10$ for (c)(d).

direction, $(0, 1)$ for d_{xy} AM, the total Hamiltonian possesses the combined symmetry of R_{sg} followed by real-space reflection with respect anti-nodal line. This symmetry protects the degeneracy of the Green functions and spectral functions: $\tilde{G}_{R,\uparrow}(\tau) = \tilde{G}_{R,\downarrow}(\tau)$ and consequently, $\tilde{N}_{R,\uparrow}(\omega) = \tilde{N}_{R,\downarrow}(\omega)$.

To further characterize the spatial distribution of the spin asymmetry, we define the integrated difference in the composite fermion Green function as

$$\begin{aligned} \Delta\tilde{G}_R &= \left(\int_0^{\beta/2} d\tau - \int_{\beta/2}^{\beta} d\tau \right) \left(\tilde{G}_{R,\uparrow}(\tau) - \tilde{G}_{R,\downarrow}(\tau) \right) \\ &= \int d\omega \left[\tilde{N}_{R,\uparrow}(\omega) - \tilde{N}_{R,\downarrow}(\omega) \right] f_{\beta}(\omega), \end{aligned} \quad (4)$$

with $f_{\beta}(\omega) = \frac{1}{\omega} \left(1 - \frac{1}{\cosh(\beta\omega/2)} \right)$ an odd function of frequency. In contrast, the sum of integrations from 0 to $\beta/2$ and from $\beta/2$ to β is just the difference between $\tilde{G}_{R,\uparrow}(\omega = 0)$ and $\tilde{G}_{R,\downarrow}(\omega = 0)$, yielding 0 due to the symmetry $\tilde{N}_{R,\uparrow}(\omega) = \tilde{N}_{R,\downarrow}(-\omega)$. $\Delta\tilde{G}_R$ vanishes in the presence of TR symmetry [63], and acts as a proxy for the asymmetry between up and down local density of states. A key point is that this quantity can be computed from the imaginary-time Green function without

having to use analytical continuation. The dependence of $\Delta\tilde{G}$ on \mathbf{R} is shown in Fig. 2(c) along with its Fourier transformation in terms of (k_x, k_y) . Here, we carry out a simulation for each value of \mathbf{R} and then carry out the Fourier transformation. We see that $\Delta\tilde{G}_R$ changes sign under a $\pi/2$ rotation, resulting into nodal lines along the directions $\delta x = 0$ and $\delta y = 0$, and along $k_x, k_y = 0$ in its Fourier transform, which directly reflects the underlying d_{xy} symmetry of the AM background.

Due to the breaking of TR symmetry, static magnetic moments appear in the presence of two impurities. The rotation of π around the z -axis with respect to the middle point of two impurities exchanges them, hence, the moments on the impurity sites should be the same. In Fig. 2(d), the value of $\langle \hat{S}_R^z \rangle$ is depicted as a function of \mathbf{R} . The AM symmetry of the band is also captured by the anisotropy in the spin fluctuations between two impurities. Consider,

$$C_R^{x(z)}(\tau) = \left\langle T_{\tau} \hat{S}_0^{x(z)}(\tau) \hat{S}_R^{x(z)} \right\rangle - \left\langle \hat{S}_0^{x(z)} \right\rangle \left\langle \hat{S}_R^{x(z)} \right\rangle, \quad (5)$$

then we define the spin anisotropy as the difference between the equal time spin-spin correlation functions as $\Delta C_R = C_R^x(0^+) - C_R^z(0^+)$, which exhibits nodal behavior along the x or y directions, consistent with the d_{xy} -wave symmetry as shown in Fig. 2(d), where the equal-time convention is taken in the limit of $\tau \rightarrow 0^+$. This follows from Eq. (2) and the restoration of the SU(2) spin symmetry for impurities along a nodal line. In the End Matter similar computations are carried out for the $d_{x^2-y^2}$ AM symmetry.

The AM term has important consequences on the nature of the RKKY interaction. Adopting a combined spin and fermion coherent state path integral formulation of the Kondo model, one can integrate out the fermionic degrees of freedom. The second-order perturbation theory in the Kondo coupling yields the RKKY interaction that reads

$$\begin{aligned} S_{\text{RKKY}} &= \frac{J_K^2 s^2}{2} \int_0^{\beta} d\tau \int_0^{\beta} d\tau' n_{\mathbf{0},\mu}(\tau) C_R^{0,\mu}(\tau - \tau') \\ &\quad \times n_{\mathbf{R},\mu}(\tau'), \end{aligned} \quad (6)$$

where $\mathbf{n}_{\mu}(\tau)$ is a spin coherent state, and $C_R^0(\tau)$ is the conduction electron spin correlation tensor evaluated in the non-interacting limit. Owing to the U(1) spin symmetry of the AM band structure, it is diagonal and differs in its xy and z components, i.e., $C^{0,x} = C^{0,y} \neq C^{0,z}$. Due to the nesting properties of the conduction electron Fermi surfaces for spin-up and spin-down components, the transverse susceptibility $\chi^{0,x}$ diverges logarithmically at the nesting vector $\mathbf{Q} = (\pi, \pi)$ as a function of temperature. The longitudinal susceptibility $\chi^{0,z}$ on the other hand shows no such divergence.

In the interacting QMC simulations, the spatial Fourier transform of $C_R^x(0^+)$ exhibits a pronounced max-

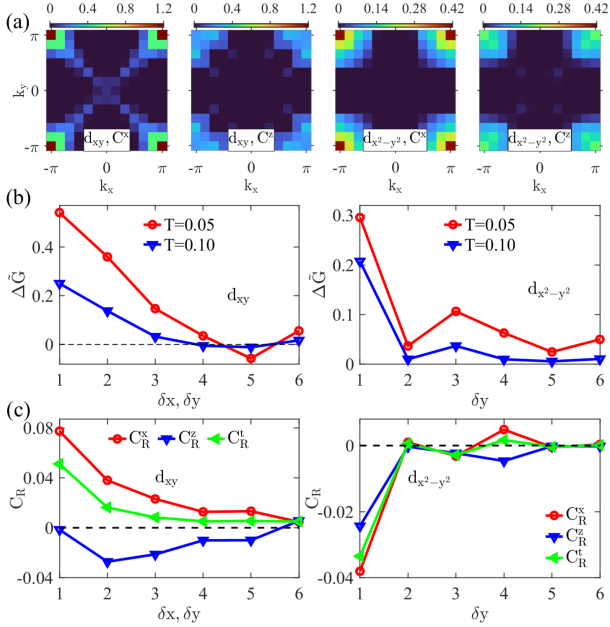


FIG. 3. The RKKY interaction at $J_K = 2$ and $t' = 0.4$. (a) Spatial Fourier transform of the equal-time spin correlation functions $C^{x,z}(0^+)$ between two impurities for both the d_{xy} and $d_{x^2-y^2}$ AM cases. (b) Distance dependence of the composite fermion Green function difference $\Delta\tilde{G}_R$ for the d_{xy} and $d_{x^2-y^2}$ cases at $T = 0.05$, 0.10. (c) Distance dependence of the spin correlation $C^{x,z}(0^+)$ between impurities and $C_R^t(0^+) = \frac{1}{3}[2C_R^x(0^+) + C_R^z(0^+)]$. The direction analyzed for d_{xy} case is along the diagonal $x = y$ direction, whereas for the $d_{x^2-y^2}$ case it is along the y -axis. We note $T = 0.1$, 0.05 for (a), (c), respectively.

imum at the wave vector $\mathbf{Q} = (\pi, \pi)$, and $C_Q^x(0^+)$ is significantly larger than $C_Q^z(0^+)$, as illustrated in Fig. 3(a). At $T = 0$, the RKKY interaction follows a power-law in real space such that the effect of one impurity on the other is not set by a characteristic length scale. Fig. 3(b) depicts the spin splitting of the Kondo resonance, $\Delta\tilde{G}_R$, as a function of \mathbf{R} . As the temperature decreases, the range of the splitting increases for both AM symmetries. As typical for a quantity without a characteristic length scale that fits on the considered finite site lattice, we observe strong size effects in terms of an upturn of the magnitude of the splitting at the largest distance, $\mathbf{R} = (6, 6)$, of our $L = 12$ lattice.

The anisotropy of the spin correlations along the anti-nodal directions is illustrated in Fig. 3(c). While in the x -components we observe (anti)-ferromagnetic correlation between sites on (different) same sub-lattices, the z -component shows dominant anti-ferromagnetic correlations. The transverse spin correlations stand in agreement with the expectations of the RKKY interaction in the absence of the AM term. On the other hand, the behavior of the longitudinal component stems from the

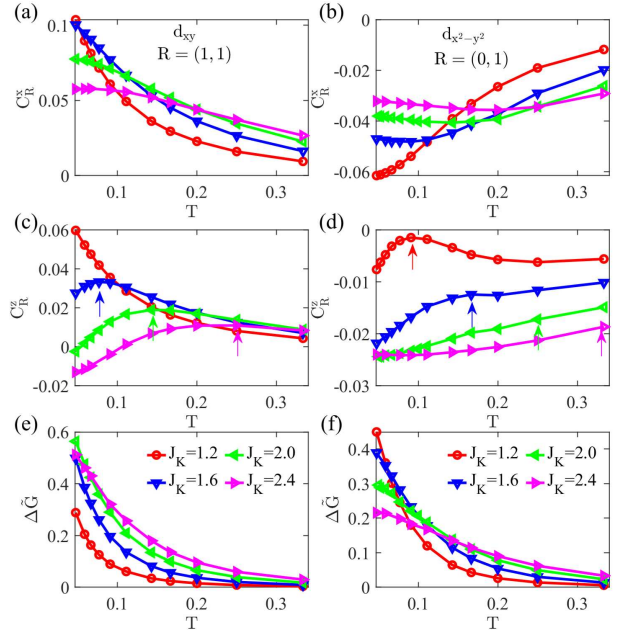


FIG. 4. Temperature evolutions for the RKKY (a, b, c,d) and for Kondo splitting (e, f) at $t' = 0.4$ for $J_K = 1.2$, 1.6, 2.0. (a,b) The x -component equal-time spin correlation function $C_R^x(0^+)$ as a function of temperature for the d_{xy} and $d_{x^2-y^2}$ cases. (c,d) Spin correlation along z direction $C_R^z(0^+)$ as a function of temperature for the d_{xy} and $d_{x^2-y^2}$ symmetry. The arrows denote the T_x scale, see main text and End Matter. (e,f) Temperature dependence of the composite fermion Green function difference $\Delta\tilde{G}_R$ at $\mathbf{R} = (1,1)$ for the d_{xy} case and at $\mathbf{R} = (0,1)$ for the $d_{x^2-y^2}$ case.

AM band structure.

Figure 4 plots the temperature dependence of spin correlations and spin splitting of the Kondo resonance for both AM symmetries and demonstrates the subtle interplay between scales of the problem. One relevant scale is T_x below which the local impurity spin susceptibility tends to saturate. When the distance between the two impurities is such that they effectively decouple, this quantity maps onto the single impurity Kondo scale. The determination of this quantity is detailed in the End Matter, and the results are plotted as arrows in Figs. 4(c)(d). Another scale is the RKKY interaction that can compete [64] or coexist [57, 60] with Kondo screening. Finally, the AM term feeds into the RKKY interaction, and provides the spin-splitting of the Kondo resonance. Below T_x and in the large J_K limit where the RKKY interaction can be omitted corresponds to the domain of validity of the large- N mean-field calculations presented in the Supplemental Material.

For the $d_{x^2-y^2}$ symmetry, see Figs. 4(b)(d)(f), we can resolve T_x for all considered values of J_K . This stems from the fact that the density of states of the AM band structure shows a van Hove singularity at the Fermi en-

ergy. In the low temperature regime $T/T_\chi \ll 1$ we observe i) the anisotropy between the transverse, Fig. 4(b), and longitudinal Fig. 4(d), spin correlations is the biggest at small J_K where the RKKY interaction dominates over the Kondo scale [64] and ii) the spin-splitting of the Kondo resonance decreases as a function of growing values of J_K . This behavior follows from the observation that the effective magnetic field perceived by the impurity spin decreases when measured in units of T_χ . On the other hand $T/T_\chi > 1$ we note that i) $\Delta\tilde{G}$ still takes a finite value and grows as a function of J_K ii) the spin anisotropy is much smaller and dominated by the AM band structure.

For d_{xy} symmetry, the van Hove singularity at the Fermi energy is absent and the T_χ and RKKY scales are smaller in the small J_K limit. In fact, at $J_K = 1.2, 1.6$ the presented data in Figs. 4(a)(c)(d) are dominated by the high temperature behavior discussed above, whereas $J_K = 2, 2.4$ capture high and low temperature behaviors.

Discussion.— In spin-resolved STM measurements [47, 48], the Kondo-related features can be easily identified in the differential conductance spectra. By extracting the peak heights, one can define a spin splitting parameter $\eta = \frac{h_{\uparrow} - h_{\downarrow}}{h_{\uparrow} + h_{\downarrow}}$, where $h_{\uparrow(\downarrow)}$ are the resonance peak values for spin-up and -down polarizations, respectively, located at either the positive or the negative bias. The real-space distribution of η , along with its Fourier transform, may directly reveal the symmetry characteristics of the underlying AM order. Such spatially resolved measurements can be achieved by varying the location and orientation of the second magnetic impurity. Furthermore, complementary techniques sensitive to local magnetization, such as muon-spin-rotation (μ SR), could also be employed to detect the symmetry of the AM phase.

The spectral features resemble those seen in the two-impurity Kondo problem subject to an external magnetic field. Therefore, our setup, realized in the absence of an applied magnetic field, provides a platform to explore rich Kondo phenomena of two impurities, including the singlet and triplet Kondo states[47, 49], two-stage Kondo screening [41], as well as single-impurity Kondo behavior.

Conclusion.— In summary, we have performed finite-temperature QMC simulations on the two-impurity Kondo model incorporating AM terms in the conduction band. The real-space spin splitting of the Kondo resonance reveals the symmetry associated with the AM terms. Our results provide a phase-sensitive approach for detecting AM via spin-resolved STM measurements. The two impurity Kondo system is the simplest possible model to understand the competition and intertwinement between Kondo, RKKY and AM. Further work for denser systems is left for future investigations.

Acknowledgments.— The authors thank Kun Yang, Danqing Hu, Gaopei Pan and Mengfan Wang for helpful discussions. QQ and CW are supported by Na-

tional Natural Science Foundation of China (Grants No. 12447125, No. 12234016) and the New Cornerstone Science Foundation. They also acknowledge the computation resource provided by Westlake HPC Center. TS and MR acknowledge financial support by the Deutsche Forschungsgemeinschaft (DFG, German Research Foundation) through the Würzburg-Dresden Cluster of Excellence ctqmat – Complexity, Topology and Dynamics in Quantum Matter (EXC 2147, project-id 390858490). FFA thanks financial support through the AS 120/16-2 (Project number 493886309) that is part of the collaborative research project SFB QMS funded by the Austrian Science Fund (FWF) F 86.

* wucongjun@westlake.edu.cn

† fakher.assaad@physik.uni-wuerzburg.de

- [1] C. Wu and S.-C. Zhang, Dynamic generation of spin-orbit coupling, *Phys. Rev. Lett.* **93**, 036403 (2004).
- [2] C. Wu, K. Sun, E. Fradkin, and S.-C. Zhang, Fermi liquid instabilities in the spin channel, *Phys. Rev. B* **75**, 115103 (2007).
- [3] M. Naka, S. Hayami, H. Kusunose, Y. Yanagi, Y. Motome, and H. Seo, Spin current generation in organic anti-ferromagnets, *Nature Communications* **10**, 4305 (2019).
- [4] K.-H. Ahn, A. Hariki, K.-W. Lee, and J. Kuneš, Antiferromagnetism in RuO_2 as d -wave pomeranchuk instability, *Phys. Rev. B* **99**, 184432 (2019).
- [5] S. Hayami, Y. Yanagi, and H. Kusunose, Momentum-dependent spin splitting by collinear antiferromagnetic ordering, *J. Phys. Soc. Jpn.* **88**, 123702 (2019).
- [6] L. Šmejkal, J. Sinova, and T. Jungwirth, Emerging research landscape of altermagnetism, *Phys. Rev. X* **12**, 040501 (2022).
- [7] H. Bai, Y. C. Zhang, Y. J. Zhou, P. Chen, C. H. Wan, L. Han, W. X. Zhu, S. X. Liang, Y. C. Su, X. F. Han, F. Pan, and C. Song, Efficient spin-to-charge conversion via altermagnetic spin splitting effect in antiferromagnet RuO_2 , *Phys. Rev. Lett.* **130**, 216701 (2023).
- [8] J. A. Ouassou, A. Brataas, and J. Linder, dc josephson effect in altermagnets, *Phys. Rev. Lett.* **131**, 076003 (2023).
- [9] Y. Guo, H. Liu, O. Janson, I. C. Fulga, J. van den Brink, and J. I. Facio, Spin-split collinear antiferromagnets: A large-scale ab-initio study, *Mater. Today Phys.* **32**, 100991 (2023).
- [10] S. Lee, S. Lee, S. Jung, J. Jung, D. Kim, Y. Lee, B. Seok, J. Kim, B. G. Park, L. Šmejkal, C.-J. Kang, and C. Kim, Broken Kramers degeneracy in altermagnetic MnTe , *Phys. Rev. Lett.* **132**, 036702 (2024).
- [11] J. Liu, J. Zhan, T. Li, J. Liu, S. Cheng, Y. Shi, L. Deng, M. Zhang, C. Li, J. Ding, Q. Jiang, M. Ye, Z. Liu, Z. Jiang, S. Wang, Q. Li, Y. Xie, Y. Wang, S. Qiao, J. Wen, Y. Sun, and D. Shen, Absence of altermagnetic spin splitting character in rutile oxide RuO_2 , *Phys. Rev. Lett.* **133**, 176401 (2024).
- [12] Z. Liu, M. Ozeki, S. Asai, S. Itoh, and T. Matsuda, Chiral split magnon in altermagnetic MnTe , *Phys. Rev. Lett.* **133**, 156702 (2024).
- [13] J. Ding, Z. Jiang, X. Chen, Z. Tao, Z. Liu, T. Li,

J. Liu, J. Sun, J. Cheng, J. Liu, Y. Yang, R. Zhang, L. Deng, W. Jing, Y. Huang, Y. Shi, M. Ye, S. Qiao, Y. Wang, Y. Guo, D. Feng, and D. Shen, Large band splitting in g -wave altermagnet CrSb, *Phys. Rev. Lett.* **133**, 206401 (2024).

[14] O. J. Amin, A. Dal Din, E. Golias, Y. Niu, A. Zakharov, S. C. Fromage, C. J. B. Fields, S. L. Heywood, R. B. Cousins, F. Maccherozzi, J. Krempaský, J. H. Dil, D. Kriegner, B. Kiraly, R. P. Campion, A. W. Rushforth, K. W. Edmonds, S. S. Dhesi, L. Šmejkal, T. Jungwirth, and P. Wadley, Nanoscale imaging and control of altermagnetism in MnTe, *Nature* **636**, 348 (2024).

[15] P. A. McClarty and J. G. Rau, Landau theory of altermagnetism, *Phys. Rev. Lett.* **132**, 176702 (2024).

[16] B. Lu, K. Maeda, H. Ito, K. Yada, and Y. Tanaka, φ josephson junction induced by altermagnetism, *Phys. Rev. Lett.* **133**, 226002 (2024).

[17] P. Das, V. Leeb, J. Knolle, and M. Knap, Realizing altermagnetism in Fermi-Hubbard models with ultracold atoms, *Phys. Rev. Lett.* **132**, 263402 (2024).

[18] S. A. A. Ghorashi, T. L. Hughes, and J. Cano, Altermagnetic routes to majorana modes in zero net magnetization, *Phys. Rev. Lett.* **133**, 106601 (2024).

[19] T. Sato, S. Haddad, I. C. Fulga, F. F. Assaad, and J. van den Brink, Altermagnetic anomalous Hall effect emerging from electronic correlations, *Phys. Rev. Lett.* **133**, 086503 (2024).

[20] C.-T. Liao, Y.-C. Wang, Y.-C. Tien, S.-Y. Huang, and D. Qu, Separation of inverse altermagnetic spin-splitting effect from inverse spin Hall effect in RuO₂, *Phys. Rev. Lett.* **133**, 056701 (2024).

[21] X. Zhou, W. Feng, R.-W. Zhang, L. Šmejkal, J. Sinova, Y. Mokrousov, and Y. Yao, Crystal thermal transport in altermagnetic RuO₂, *Phys. Rev. Lett.* **132**, 056701 (2024).

[22] Z. Jin, Z. Zeng, Y. Cao, and P. Yan, Skyrmiion Hall effect in altermagnets, *Phys. Rev. Lett.* **133**, 196701 (2024).

[23] X. Chen, J. Ren, Y. Zhu, Y. Yu, A. Zhang, P. Liu, J. Li, Y. Liu, C. Li, and Q. Liu, Enumeration and representation theory of spin space groups, *Phys. Rev. X* **14**, 031038 (2024).

[24] Y. Jiang, Z. Song, T. Zhu, Z. Fang, H. Weng, Z.-X. Liu, J. Yang, and C. Fang, Enumeration of spin-space groups: Toward a complete description of symmetries of magnetic orders, *Phys. Rev. X* **14**, 031039 (2024).

[25] Z. Xiao, J. Zhao, Y. Li, R. Shindou, and Z.-D. Song, Spin space groups: Full classification and applications, *Phys. Rev. X* **14**, 031037 (2024).

[26] G. Yang, Z. Li, S. Yang, J. Li, H. Zheng, W. Zhu, Z. Pan, Y. Xu, S. Cao, W. Zhao, A. Jana, J. Zhang, M. Ye, Y. Song, L.-H. Hu, L. Yang, J. Fujii, I. Vobornik, M. Shi, H. Yuan, Y. Zhang, Y. Xu, and Y. Liu, Three-dimensional mapping of the altermagnetic spin splitting in CrSb, *Nat. Commun.* **16**, 1442 (2025).

[27] B. Jiang, M. Hu, J. Bai, Z. Song, C. Mu, G. Qu, W. Li, W. Zhu, H. Pi, Z. Wei, Y.-J. Sun, Y. Huang, X. Zheng, Y. Peng, L. He, S. Li, J. Luo, Z. Li, G. Chen, H. Li, H. Weng, and T. Qian, A metallic room-temperature d -wave altermagnet, *Nat. Phys.* **21**, 754 (2025).

[28] C. Song, H. Bai, Z. Zhou, L. Han, H. Reichlova, J. H. Dil, J. Liu, X. Chen, and F. Pan, Altermagnets as a new class of functional materials, *Nat. Rev. Mater.* **10**, 473 (2025).

[29] M. Gu, Y. Liu, H. Zhu, K. Yananose, X. Chen, Y. Hu, A. Stroppa, and Q. Liu, Ferroelectric switchable altermagnetism, *Phys. Rev. Lett.* **134**, 106802 (2025).

[30] Y. Chen, X. Liu, H.-Z. Lu, and X. C. Xie, Electrical switching of altermagnetism, *Phys. Rev. Lett.* **135**, 016701 (2025).

[31] P. M. Cónsoli and M. Vojta, SU(N) altermagnetism: Lattice models, magnon modes, and flavor-split bands, *Phys. Rev. Lett.* **134**, 196701 (2025).

[32] H.-J. Lin, S.-B. Zhang, H.-Z. Lu, and X. C. Xie, Coulomb drag in altermagnets, *Phys. Rev. Lett.* **134**, 136301 (2025).

[33] X. Duan, J. Zhang, Z. Zhu, Y. Liu, Z. Zhang, I. Žutić, and T. Zhou, Antiferroelectric altermagnets: Antiferroelectricity alters magnets, *Phys. Rev. Lett.* **134**, 106801 (2025).

[34] L. V. Pupim and M. S. Scheurer, Adatom engineering magnetic order in superconductors: Applications to altermagnetic superconductivity, *Phys. Rev. Lett.* **134**, 146001 (2025).

[35] T. Sato, M. Hu, I. C. Fulga, O. Janson, J. I. Fazio, A. Stroppa, F. F. Assaad, and J. van den Brink, Ferro-spinetic altermagnets from electronic correlations, arXiv:2510.18973 (2025).

[36] M. Zhao, W.-W. Yang, X. Guo, H.-G. Luo, and Y. Zhong, Altermagnetism in heavy-fermion systems: Mean-field study on the Kondo lattice, *Phys. Rev. B* **111**, 085145 (2025).

[37] G. S. Diniz and E. Vernek, Suppressed Kondo screening in two-dimensional altermagnets, *Phys. Rev. B* **109**, 155127 (2024).

[38] Y.-L. Lee, Magnetic impurities in an altermagnetic metal, *Eur. Phys. J. B* **98**, 43 (2025).

[39] C. C. Tsuei and J. R. Kirtley, Phase-sensitive evidence for d -wave pairing symmetry in electron-doped cuprate superconductors, *Phys. Rev. Lett.* **85**, 182 (2000).

[40] R. Wiesendanger, Spin mapping at the nanoscale and atomic scale, *Rev. Mod. Phys.* **81**, 1495 (2009).

[41] C. Jayaprakash, H. R. Krishna-murthy, and J. W. Wilkins, Two-impurity Kondo problem, *Phys. Rev. Lett.* **47**, 737 (1981).

[42] B. A. Jones, C. M. Varma, and J. W. Wilkins, Low-temperature properties of the two-impurity Kondo hamiltonian, *Phys. Rev. Lett.* **61**, 125 (1988).

[43] R. M. Fye and J. E. Hirsch, Quantum Monte Carlo study of the two-impurity Kondo hamiltonian, *Phys. Rev. B* **40**, 4780 (1989).

[44] C. Sire, C. M. Varma, and H. R. Krishnamurthy, Theory of the non-Fermi-liquid transition point in the two-impurity Kondo model, *Phys. Rev. B* **48**, 13833 (1993).

[45] R.-Q. He, J. Dai, and Z.-Y. Lu, Natural orbitals renormalization group approach to the two-impurity Kondo critical point, *Phys. Rev. B* **91**, 155140 (2015).

[46] J.-J. Dong, D. Huang, and Y.-f. Yang, Mutual information, quantum phase transition, and phase coherence in Kondo systems, *Phys. Rev. B* **104**, L081115 (2021).

[47] A. Spinelli, M. Gerrits, R. Toskovic, B. Bryant, M. Ternes, and A. F. Otte, Exploring the phase diagram of the two-impurity Kondo problem, *Nat. Commun.* **6**, 10046 (2015).

[48] K. von Bergmann, M. Ternes, S. Loth, C. P. Lutz, and A. J. Heinrich, Spin polarization of the split Kondo state, *Phys. Rev. Lett.* **114**, 076601 (2015).

[49] V. L. Campo and L. N. Oliveira, Thermodynamics for the two-impurity Kondo model, *Phys. Rev. B* **70**, 153401 (2004).

[50] R. Blankenbecler, D. J. Scalapino, and R. L. Sugar, Monte Carlo calculations of coupled boson-fermion systems., *Phys. Rev. D* **24**, 2278 (1981).

[51] S. White, D. Scalapino, R. Sugar, E. Loh, J. Gubernatis, and R. Scalettar, Numerical study of the two-dimensional hubbard model, *Phys. Rev. B* **40**, 506 (1989).

[52] F. Assaad and H. Evertz, World-line and determinantal quantum Monte Carlo methods for spins, phonons and electrons, in *Computational Many-Particle Physics*, Lecture Notes in Physics, Vol. 739, edited by H. Fehske, R. Schneider, and A. Weiße (Springer, Berlin Heidelberg, 2008) pp. 277–356.

[53] P. Coleman, *Introduction to Many-body Physics* (Cambridge University press., Cambridge, 2015).

[54] C. Wu and S.-C. Zhang, Sufficient condition for absence of the sign problem in the fermionic quantum Monte Carlo algorithm, *Phys. Rev. B* **71**, 155115 (2005).

[55] T. Sato, F. F. Assaad, and T. Grover, Quantum Monte Carlo simulation of frustrated Kondo lattice models, *Phys. Rev. Lett.* **120**, 107201 (2018).

[56] F. F. Assaad, Quantum Monte Carlo simulations of the half-filled two-dimensional Kondo lattice model, *Phys. Rev. Lett.* **83**, 796 (1999).

[57] S. Capponi and F. F. Assaad, Spin and charge dynamics of the ferromagnetic and antiferromagnetic two-dimensional half-filled Kondo lattice model, *Phys. Rev. B* **63**, 155114 (2001).

[58] F. F. Assaad, M. Bercx, F. Goth, A. Götz, J. S. Hofmann, E. Huffman, Z. Liu, F. P. Toldin, J. S. E. Portela, and J. Schwab, The ALF (Algorithms for Lattice Fermions) project release 2.4. Documentation for the auxiliary-field quantum Monte Carlo code, *SciPost Phys. Codebases* , 1 (2025).

[59] T. A. Costi, Kondo effect in a magnetic field and the magnetoresistivity of Kondo alloys, *Phys. Rev. Lett.* **85**, 1504 (2000).

[60] B. Danu, Z. Liu, F. F. Assaad, and M. Raczkowski, Zooming in on heavy fermions in Kondo lattice models, *Phys. Rev. B* **104**, 155128 (2021).

[61] M. Raczkowski, B. Danu, and F. F. Assaad, Breakdown of heavy quasiparticles in a honeycomb Kondo lattice: A quantum Monte Carlo study, *Phys. Rev. B* **106**, L161115 (2022).

[62] M. Jarrell and J. E. Gubernatis, Bayesian inference and the analytic continuation of imaginary-time quantum Monte Carlo data, *Phys. Rep.* **269**, 133 (1996).

[63] This includes the generic two impurity problem on a metallic surface where spin-orbit coupling is present.

[64] S. Doniach, The Kondo lattice and weak antiferromagnetism, *Physica B+C* **91**, 231 (1977).

[65] N. Andrei, Diagonalization of the Kondo hamiltonian, *Phys. Rev. Lett.* **45**, 379 (1980).

[66] A. Hewson, *The Kondo Problem to Heavy Fermions*, Cambridge History of Medicine (Cambridge University Press, 1993).

End Matter

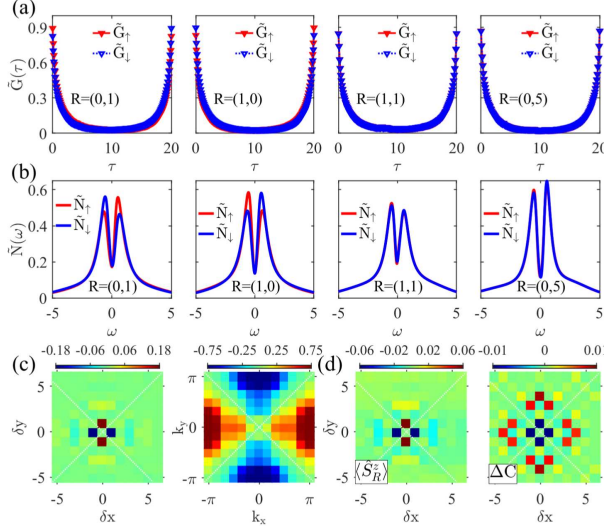


FIG. 5. $d_{x^2-y^2}$ altermagnetic symmetry at $J_K = 2$ and $t' = 0.4$. (a) Imaginary-time Green function of the composite fermion $\tilde{G}_R(\tau)$ at different displacement vector $\mathbf{R} = (\delta x, \delta y)$ between two impurities. (b) Spectral function $\tilde{N}_R(\omega)$ at different values of \mathbf{R} . (c) Real-space distribution of ΔG_R defined in Eq. (4) along with its Fourier transform. (d) The local magnetic moment $\langle \hat{S}_R^z \rangle$ and the real-space equal-time spin correlation functions between two impurities exhibit anisotropy, characterized by $\Delta C_R = C_R^x(0^+) - C_R^z(0^+)$. Temperatures are set to $T = 0.05$ for panels (a) and (b), and $T = 0.10$ for panels (c) and (d).

Symmetries of the single particle Green function.— Here we investigate the spin symmetry of the single particle Green function.

We will consider the real space Green function,

$$G_{\sigma\sigma'}(i - j, \tau) = \langle T \hat{c}_{i,\sigma'}^\dagger(\tau) \hat{c}_{j,\sigma}(0) \rangle. \quad (\text{A.1})$$

and show that if i and j are on a nodal line, then the Green function is spin independent.

Firstly, let $\hat{U}(e_{x(y)}, \pi)$ be an global SU(2) rotation around the $x(y)$ -axis with angle π , and \hat{T}_m be the mirror symmetry on the nodal lines. That is $(1, 1)$, $(1, -1)$ for $d_{x^2-y^2}$ and $(1, 0)$, $(0, 1)$ for d_{xy} . We define combined transformations

$$\hat{T}_x = \hat{U}(e_x, \pi) \hat{T}_m, \quad \hat{T}_y = \hat{U}(e_y, \pi) \hat{T}_m, \quad (\text{A.2})$$

where

$$\hat{T}_x \hat{c}_i^\dagger \hat{T}_x^{-1} = \hat{c}_{T_m(i)}^\dagger U(e_x, \pi), \quad (\text{A.3})$$

$$\hat{T}_y \hat{c}_i^\dagger \hat{T}_y^{-1} = \hat{c}_{T_m(i)}^\dagger U(e_y, \pi), \quad (\text{A.4})$$

with $U(e_x, \pi) = e^{i\pi\sigma_x/2}$ and $U(e_y, \pi) = e^{i\pi\sigma_y/2}$. Furthermore, one will show that:

$$[\hat{H}_0, \hat{T}_x] = [\hat{H}_0, \hat{T}_y] = 0. \quad (\text{A.5})$$

Let us now assume that i and j both lie on a nodal line such that $T_m(i) = i$ and $T_m(j) = j$. We expand the 2 matrix of $G(i - j, \tau)$ in terms of the identity and three Pauli matrices as

$$G(i - j, \tau) = a_0 I + a_i \sigma_i. \quad (\text{A.6})$$

The \hat{T}_x symmetry ensures that $a_y = a_z = 0$ and the \hat{T}_y symmetry ensures that $a_x = a_z = 0$, hence, only $a_0 \neq 0$ such that the Green function along a nodal line has no spin dependence.

Generically, the Green function will be diagonal in the spin indices. This follows from the U(1) spin-rotational symmetry about the z -axis that leaves \hat{H}_0 invariant.

Real space spin splitting of the $d_{x^2-y^2}$ symmetry.— The case of the $d_{x^2-y^2}$ -type altermagnetism can be analyzed within the same framework. The key distinction lies in the symmetry of the induced quantities: $\Delta \tilde{G}_R$, $\langle \hat{S}_R^z \rangle$ and $\Delta \chi_R$ now exhibit nodal lines along the diagonal-direction, reflecting a characteristic $d_{x^2-y^2}$ symmetry, as shown in Fig. 5.

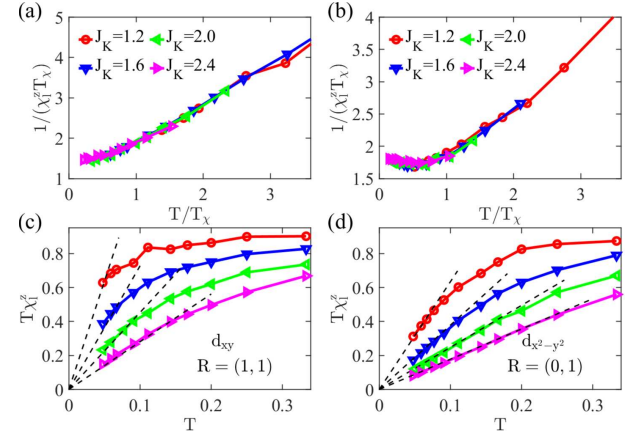


FIG. 6. Local spin susceptibility for d_{xy} case (a)(c) with $\mathbf{R} = (1, 1)$ and $d_{x^2-y^2}$ symmetry (b)(d) with $\mathbf{R} = (0, 1)$. (a)(c) Temperature dependence of the local spin susceptibility χ_i^z for $J_K = 1.2, 1.6, 2.0, 2.4$, for d_{xy} and $d_{x^2-y^2}$ respectively. (b)(d) Temperature dependence of $T\chi_i^z$ for $J_K = 1.2, 1.6, 2.0, 2.4$, for d_{xy} and $d_{x^2-y^2}$ respectively.

Kondo screening.— We further analyze the effect of the altermagnetic term on Kondo screening. As mention in the main text, since the altermagnetic term acts as a momentum-dependent effective magnetic field, rather than a uniform Zeeman field, it does not induce a breakdown of the single impurity Kondo effect. For the two impurity case we have seen in the main text that impurities develop a finite magnetization provided that they are not on a nodal line. This is very similar to the Kondo effect in a magnetic field, and we will inspire ourselves from this piece of physics [59, 65, 66] to interpret our data.

We calculate the local spin correlation function $C_l^{x(z)}(\tau) = \langle T_\tau \hat{S}_0^{x(z)}(\tau) \hat{S}_0^{x(z)} \rangle - \langle \hat{S}_0^{x(z)} \rangle^2$ and its imaginary-time integral, $\chi_l^{x(z)} = \int_0^\beta d\tau C_l^{x(z)}(\tau)$, to characterize Kondo screening. The latter quantity corresponds to the local spin susceptibility.

As shown in Fig. 6(a), the data for χ_l^z seemingly collapses onto a single curve when rescaled by an appropriate characteristic temperature T_χ for $J_K = 1.2, 1.6, 2.0, 2.4$ for the d_{xy} case with $\mathbf{R} = (1, 1)$. Similar results are plotted in Fig. 6(b) for the $d_{x^2-y^2}$ case at $\mathbf{R} = (0, 1)$. As mentioned above, we would like to interpret these results in the framework of the single impurity Kondo model in a magnetic field. Here, the local spin susceptibility satisfies the scaling relation $T_K \chi_l^z = f(T/T_K, B/T_K)$ with f a scaling function [65, 66]. When the two impurities are very far apart, this form certainly holds since the impurities decouple. Furthermore, in this limit the effective magnetic field vanishes, leading to a data collapse of $T_K \chi_l^z$ versus T/T_K . As the distance between the two impurities is reduced we expect to observe correction to scaling when plotting $T_K \chi_l^z$ versus T/T_K at constant magnetic field (i.e. con-

stant value of t'). The RKKY interaction is equally expected to yield corrections to scaling. As apparent from the data in Figs. 6(a)(b) such correction to scaling seem to be small, and/or may be included in a redefinition of the Kondo scale, T_χ .

The characteristic temperature T_χ can be identified from the deviation from linear behavior for $T \chi_l^z$ shown in Figs. 6(c)(d). Furthermore, $\lim_{T \rightarrow 0} T \chi_l^z \rightarrow 0$, indicating the absence of a local magnetic moment at zero temperature.

Together, these results demonstrate that Kondo screening persists even in the presence of altermagnetic terms. In the Supplemental Material, we show that the transverse component χ_l^x exhibits nearly identical behavior, with only a negligible differences compared to χ_l^z .

The T_χ scale in the small J_K limit turns out to be much smaller for the d_{xy} case as compared to the $d_{x^2-y^2}$ symmetry. We understand this in terms of the local density of states: for the $d_{x^2-y^2}$ (d_{xy}) symmetry we do (not) observe a Van-Hove singularity at the Fermi energy. In particular, and as apparent from Fig. 6(c) it becomes hard to pin down a value of T_χ within our accessible temperature range and lattice size for the d_{xy} case at $J_K \lesssim 1.6$.

Revealing altermagnetic Fermi surfaces with two Kondo impurities

Supplemental Material

I. Quantum Monte Carlo Simulations of the Multi-Impurity Kondo Model

The simulations of the $SU(N)$ multi-impurity Kondo model are carried out along the lines of the Algorithms for Lattice fermions [58] implementation of the Kondo lattice model. The Hamiltonian can be written as

$$H = H_c + H_f + H_{cf}, \quad (S1)$$

where the individual terms are given by

$$\begin{aligned} H_c &= -t \sum_i \left(\hat{c}_{i\sigma}^\dagger \hat{c}_{i+\hat{x}\sigma} + \hat{c}_{i\sigma}^\dagger \hat{c}_{i+\hat{y}\sigma} + h.c. \right) - t' \sum_{i\sigma} \text{sgn}(\sigma) \left(\hat{c}_{i\sigma}^\dagger \hat{c}_{i+2\hat{x}\sigma} - \hat{c}_{i\sigma}^\dagger \hat{c}_{i+2\hat{y}\sigma} + h.c. \right), \\ H_f &= \frac{U_f}{N} \sum_l \left(\hat{n}_l^f - \frac{N}{2} \right)^2, \quad H_{cf} = \frac{2J_K}{N} \sum_l \sum_{a=1}^{N^2-1} \hat{T}_l^{a,c} \hat{T}_l^{a,f}, \end{aligned} \quad (S2)$$

The operators appearing in the interaction term are defined as

$$\hat{T}_l^{a,c} = \sum_{\sigma, \sigma'} \hat{c}_{l\sigma}^\dagger T_{\sigma\sigma'}^a \hat{c}_{l\sigma'}, \quad \hat{T}_l^{a,f} = \sum_{\sigma, \sigma'} \hat{f}_{l\sigma}^\dagger T_{\sigma\sigma'}^a \hat{f}_{l\sigma'}, \quad \hat{n}_l^f = \sum_{\sigma=1}^N \hat{f}_{l\sigma}^\dagger \hat{f}_{l\sigma}, \quad \hat{n}_l^c = \sum_{\sigma=1}^N \hat{c}_{l\sigma}^\dagger \hat{c}_{l\sigma}. \quad (S3)$$

The hybridization term can be recast in the form

$$H_{cf} = -\frac{J_K}{4N} \sum_l \left[(\hat{D}_l^\dagger + \hat{D}_l)^2 + (i\hat{D}_l^\dagger - i\hat{D}_l)^2 \right] + \frac{J_K}{4} n_{imp}, \quad (S4)$$

where we have employed the completeness relation

$$\sum_a \hat{T}_{\alpha\beta}^a \hat{T}_{\alpha'\beta'}^a = \frac{1}{2} \left(\delta_{\alpha\beta'} \delta_{\alpha'\beta} - \frac{1}{N} \delta_{\alpha\beta} \delta_{\alpha'\beta'} \right), \quad (S5)$$

and introduced the operators

$$\hat{D}_l^\dagger = \sum_{\sigma=1}^N \hat{c}_{l\sigma}^\dagger \hat{f}_{l\sigma}, \quad \hat{D}_l = \sum_{\sigma=1}^N \hat{f}_{l\sigma}^\dagger \hat{c}_{l\sigma}. \quad (S6)$$

For the $SU(2)$ case, the QMC-related Hamiltonian takes the form

$$H = H_c + H_f + H_{cf}, \quad (S7)$$

with the individual contributions given by

$$\begin{aligned} H_c &= -t \sum_i \left(\hat{c}_{i\sigma}^\dagger \hat{c}_{i+\hat{x}\sigma} + \hat{c}_{i\sigma}^\dagger \hat{c}_{i+\hat{y}\sigma} + h.c. \right) - t' \sum_{i\sigma} \text{sgn}(\sigma) \left(\hat{c}_{i\sigma}^\dagger \hat{c}_{i+2\hat{x}\sigma} - \hat{c}_{i\sigma}^\dagger \hat{c}_{i+2\hat{y}\sigma} + h.c. \right), \\ H_f &= \frac{U_f}{2} \sum_l (\hat{f}_{l\uparrow}^\dagger \hat{f}_{l\uparrow} + \hat{f}_{l\downarrow}^\dagger \hat{f}_{l\downarrow} - 1)^2, \quad H_{cf} = -\frac{J_K}{8} \sum_l \left[\sum_{\sigma} \left(\hat{c}_{l\sigma}^\dagger \hat{f}_{l\sigma} + \hat{f}_{l\sigma}^\dagger \hat{c}_{l\sigma} \right) \right]^2. \end{aligned}$$

After applying the Trotter decomposition, performing the discrete Hubbard–Stratonovich (HS) transformation, and integrating out the conduction electrons, the system becomes amenable to quantum Monte Carlo (QMC) simulations. Under the HS transformation, the interaction terms in the action are rewritten as

$$S_f^{lk} = \frac{U_f \Delta\tau}{2} (f_{lk\uparrow}^\dagger f_{lk\uparrow} + f_{lk\downarrow}^\dagger f_{lk\downarrow} - 1)^2 \rightarrow \frac{U_f \Delta\tau}{2} \left[\lambda_{lk}^2 - 2i\lambda_{lk} (f_{lk\uparrow}^\dagger f_{lk\uparrow} + f_{lk\downarrow}^\dagger f_{lk\downarrow} - 1) \right], \quad (S8)$$

and

$$S_{cf}^{lk} = -\frac{J_K \Delta \tau}{8} \left[\sum_{\sigma} (c_{lk\sigma}^{\dagger} f_{lk\sigma} + f_{lk\sigma}^{\dagger} c_{lk\sigma}) \right]^2 \rightarrow \frac{J_K \Delta \tau}{8} \left[V_{lk}^2 + 2V_{lk} \sum_{\sigma} (c_{lk\sigma}^{\dagger} f_{lk\sigma} + f_{lk\sigma}^{\dagger} c_{lk\sigma}) \right]. \quad (\text{S9})$$

Here, l denotes the impurity site, k labels the imaginary-time slice τ_k , λ_{lk} represents the onsite density field, and V_{lk} denotes the onsite hybridization field.

We then employ the following approximation formula:

$$\int_{-\infty}^{\infty} dx e^{-x^2 - 2x\sqrt{\alpha}b} \approx \frac{\sqrt{\pi}}{4} \sum_{n=\pm 1, \pm 2} \gamma(n) e^{-\eta(n)\sqrt{\alpha}b}, \quad (\text{S10})$$

where the coefficients are defined as

$$\gamma(\pm) = 1 + \frac{\sqrt{6}}{3}, \quad \gamma(\pm 2) = 1 - \frac{\sqrt{6}}{3}, \quad \eta(\pm) = \pm \sqrt{2(3 - \sqrt{6})}, \quad \eta(\pm 2) = \pm \sqrt{2(3 + \sqrt{6})}. \quad (\text{S11})$$

After this transformation, the auxiliary fields λ_{lk} and V_{lk} take only discrete values given by $\eta(\pm 1, \pm 2)$, with the corresponding discrete indices n_{lk} , $v_{lk} = \pm 1, \pm 2$. For the term S_{cf}^{lk} , the parameters are identified as

$$\sqrt{\alpha} = f_{lk\uparrow}^{\dagger} f_{lk\uparrow} + f_{lk\downarrow}^{\dagger} f_{lk\downarrow} - 1, \quad b = i\sqrt{U_f \Delta \tau / 2}. \quad (\text{S12})$$

Similarly, for the Kondo part S_{cf}^{lk} ,

$$\sqrt{\alpha} = \sum_{\sigma} (c_{lk\sigma}^{\dagger} f_{lk\sigma} + f_{lk\sigma}^{\dagger} c_{lk\sigma}), \quad b = \sqrt{J_K \Delta \tau / 8}. \quad (\text{S13})$$

Under the partial particle-hole transformation,

$$c_{lk\uparrow} \rightarrow c_{lk\uparrow}, \quad c_{lk\downarrow} \rightarrow (-1)^l c_{lk\downarrow}^{\dagger}, \quad f_{lk\uparrow} \rightarrow f_{lk\uparrow}, \quad f_{lk\downarrow} \rightarrow -(-1)^l f_{lk\downarrow}^{\dagger}, \quad (\text{S14})$$

the interaction terms transform as

$$\begin{aligned} i\sqrt{U_f \Delta \tau / 2} \eta(n_{lk}) (f_{lk\downarrow}^{\dagger} f_{lk\downarrow} - \frac{1}{2}) &\rightarrow -i\sqrt{U_f \Delta \tau / 2} \eta(n_{lk}) (f_{lk\downarrow}^{\dagger} f_{lk\downarrow} - \frac{1}{2}), \\ \sqrt{J_K \Delta \tau / 8} \eta(v_{lk}) (c_{lk\downarrow}^{\dagger} f_{lk\downarrow} + f_{lk\downarrow}^{\dagger} c_{lk\downarrow}) &\rightarrow \sqrt{J_K \Delta \tau / 8} \eta(v_{lk}) (c_{lk\downarrow}^{\dagger} f_{lk\downarrow} + f_{lk\downarrow}^{\dagger} c_{lk\downarrow}). \end{aligned} \quad (\text{S15})$$

Similarly, the kinetic terms transform as

$$\begin{aligned} -t \sum_i (c_{ik\downarrow}^{\dagger} c_{i+\hat{x}, k\downarrow} + c_{ik\downarrow}^{\dagger} c_{i+\hat{y}, k\downarrow} + h.c.) &\rightarrow -t \sum_i (c_{ik\downarrow}^{\dagger} c_{i+\hat{x}, k\downarrow} + c_{ik\downarrow}^{\dagger} c_{i+\hat{y}, k\downarrow} + h.c.) \\ t' \sum_i (c_{ik\downarrow}^{\dagger} c_{i+2\hat{x}, k\downarrow} - c_{ik\downarrow}^{\dagger} c_{i+2\hat{y}, k\downarrow} + h.c.) &\rightarrow -t' \sum_i (c_{ik\downarrow}^{\dagger} c_{i+2\hat{x}, k\downarrow} - c_{ik\downarrow}^{\dagger} c_{i+2\hat{y}, k\downarrow} + h.c.). \end{aligned} \quad (\text{S16})$$

For the d_{xy} altermagnetic terms, the transformation proceeds analogously. As a consequence, the matrix representation for spin-down c and f fermions becomes the Hermitian conjugate of the corresponding spin-up matrix. This guarantees the absence of negative sign problem in the QMC simulations.

II. Hybridization Function and Saddle Point

The Kondo coupling is expressed as

$$J_K \sum_l \hat{S}_l \cdot \hat{s}_l, \quad (\text{S17})$$

where $\hat{S}_l = \frac{1}{2} \sum_{\alpha\beta} \hat{f}_{l\alpha}^{\dagger} \boldsymbol{\sigma}_{\alpha\beta} \hat{f}_{l\beta}$ is the local spin operator in the pseudo-fermion representation, subject to the local constraint $\sum_{\alpha} \hat{f}_{l\alpha}^{\dagger} \hat{f}_{l\alpha} = 1$.

Within the path-integral formalism of the multi-impurity Kondo model, the partition function takes the form

$$Z = \int D[c^\dagger, c, f^\dagger, f, \lambda] e^{-S}, \quad (\text{S18})$$

with the action

$$\begin{aligned} S = & \int_0^\beta d\tau \left[\sum_{\mathbf{k}\sigma} c_{\mathbf{k}\sigma}^\dagger(\tau) (\partial_\tau + \epsilon_{\mathbf{k}\sigma}) c_{\mathbf{k}\sigma}(\tau) + \sum_l f_{l\sigma}^\dagger(\tau) (\partial_\tau + i\lambda_l) f_{l\sigma}(\tau) \right] \\ & - \int_0^\beta d\tau \frac{J_K}{2} \sum_l \left(\sum_\beta c_{l\beta}^\dagger(\tau) f_{l\beta}(\tau) \right) \left(\sum_\alpha f_{l\alpha}^\dagger(\tau) c_{l\alpha}(\tau) \right) - \sum_l i\lambda_l, \end{aligned} \quad (\text{S19})$$

where λ_l is introduced to enforce the single-occupancy the constraint.

By applying a HS transformation, we introduce the hybridization field V_l , leading to

$$-\frac{J_K}{2} \left(\sum_\beta c_{l\beta}^\dagger f_{l\beta} \right) \left(\sum_\alpha f_{l\alpha}^\dagger c_{l\alpha} \right) \rightarrow \frac{2\bar{V}_l V_l}{J_K} + \left(\sum_\alpha f_{l\alpha}^\dagger c_{l\alpha} \right) V_l + \bar{V}_l \left(\sum_\alpha c_{l\alpha}^\dagger f_{l\alpha} \right). \quad (\text{S20})$$

Accordingly, the action can be rewritten as

$$S[\bar{V}, V, c^\dagger, c, f^\dagger, f, \lambda] = \int_0^\beta d\tau \left[\sum_\sigma \psi_\sigma^\dagger (\partial_\tau + h^\sigma) \psi_\sigma + \sum_j \frac{2|V_j(\tau)|^2}{J} \right], \quad (\text{S21})$$

where

$$\psi_\sigma^\dagger = (c_{\mathbf{k}_1\sigma}^\dagger, \dots, c_{\mathbf{k}_i\sigma}^\dagger, \dots, c_{\mathbf{k}_n\sigma}^\dagger, f_{1\sigma}^\dagger, \dots, f_{j\sigma}^\dagger, \dots, f_{n_0\sigma}^\dagger),$$

and

$$h_\sigma = \begin{pmatrix} E^\sigma & M^\dagger \\ M & \Lambda \end{pmatrix}, \quad M_{i,j} = \frac{V_j}{\sqrt{n}} e^{i\mathbf{k}_i R_j}, \quad E_{ij}^\sigma = \delta_{ij} \epsilon_{\mathbf{k}_i \sigma}, \quad \Lambda_{ij} = i\delta_{ij} \lambda_i. \quad (\text{S22})$$

By employing the Gaussian integral identity

$$\int \mathcal{D}(\bar{\phi}, \phi) e^{-\bar{\phi}^T A \phi + \bar{v}^T \phi + \bar{\phi}^T v} = \det(A) e^{-\bar{v} A^{-1} v}, \quad (\text{S23})$$

and assuming that the hybridization fields are static, we can integrate out the conduction electrons to obtain the effective action for the f electrons. The partition function then becomes

$$Z = \int \mathcal{D}[\bar{V}, V, f^\dagger, f, \lambda] e^{-S_f}, \quad (\text{S24})$$

where

$$S_f = \sum_{ln\sigma} f_{l\sigma}^\dagger (i\omega_n) (-i\omega_n + i\lambda_l) f_{l\sigma}(i\omega_n) + \sum_{njl\sigma} f_{j\sigma}^\dagger (i\omega_n) f_{l\sigma}(i\omega_n) \Delta_{jl}^\sigma(i\omega_n) + \sum_l \frac{2\bar{V}_l V_l}{J_K}, \quad (\text{S25})$$

and the hybridization function is given by

$$\Delta_{jl}^\sigma(i\omega_n) = \sum_{\mathbf{k}} \frac{\bar{V}_j V_l e^{i\mathbf{k} \cdot (\mathbf{R}_j - \mathbf{R}_l)}}{-i\omega_n + \epsilon_{\mathbf{k}\sigma}}. \quad (\text{S26})$$

For the single-impurity case, the hybridization function reduces to

$$\Delta^\sigma(i\omega_n) = \sum_{\mathbf{k}} \frac{|V|^2}{-i\omega_n + \epsilon_{\mathbf{k}\sigma}}. \quad (\text{S27})$$

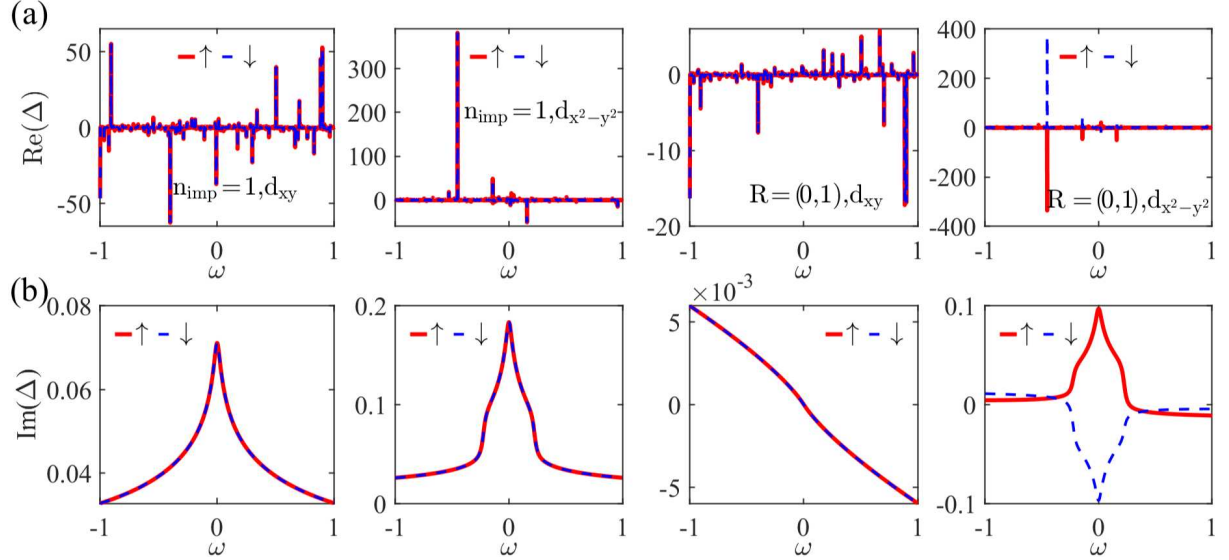


FIG. S1. (a) Real (Re) and (b) imaginary (Im) parts of the hybridization function $\Delta(\omega)$ for the single- and two-impurity Kondo models with altermagnetic terms, obtained with $t' = 0.4$ and $V_l = 0.5$. The vector $\mathbf{R} = (0, 1)$ denotes the spatial separation between the two impurities.

Since the dispersion satisfies $\epsilon_{\mathbf{k}\sigma} \rightarrow \epsilon_{\mathbf{k}\bar{\sigma}}$ under the C_{4z} rotation, the hybridization function obeys the relation $\Delta^\sigma(i\omega_n) = \Delta^{\bar{\sigma}}(i\omega_n)$, as illustrated in Fig. S1(a)(b). It should be noted that the function is plotted after analytic continuation, $i\omega_n \rightarrow \omega + i\delta$. Consequently, the absence of spin splitting in the hybridization function enforces a spin-degenerate spectral function for both the local f electrons and the conduction c electrons.

For the two-impurity model, the diagonal components Δ_{11}^σ and Δ_{22}^σ are spin independent, whereas the off-diagonal components Δ_{12}^σ and Δ_{21}^σ acquire spin dependence. This spin asymmetry in the off-diagonal terms gives rise to spin splitting in the spectral functions of both the local f electrons and the conduction c electrons. For the case $\mathbf{R} = (0, 1)$, the mirror symmetry M_{yz} transforms the dispersion as $\epsilon_{\mathbf{k}\sigma} \rightarrow \epsilon_{\mathbf{k}\bar{\sigma}}$ in the d_{xy} case, while leaving it invariant $\epsilon_{\mathbf{k}\sigma} \rightarrow \epsilon_{\mathbf{k}\sigma}$ in the $d_{x^2-y^2}$ case, resulting in spin degeneracy for the d_{xy} altermagnetic symmetry, as shown in Fig. S1(a)(b). Similarly, when $\mathbf{R} = (1, 1)$, mirror symmetry along the diagonal direction ensures spin degeneracy for the $d_{x^2-y^2}$ case, whereas spin splitting persists in the d_{xy} case.

The local Coulomb interaction of the f electrons enforces the single-occupancy constraint but does not alter the functional form of the hybridization function.

III. RKKY Interaction

The two-impurity Kondo model can be expressed in momentum space as

$$H = \sum_{\mathbf{k}\sigma} \hat{c}_{\mathbf{k}\sigma}^\dagger \epsilon_{\mathbf{k}\sigma} \hat{c}_{\mathbf{k}\sigma} + J_K \hat{\mathbf{S}}_0 \cdot \hat{\mathbf{s}}_0 + J_K \hat{\mathbf{S}}_{\mathbf{R}} \cdot \hat{\mathbf{s}}_{\mathbf{R}}, \quad (\text{S28})$$

where the dispersion relation is given by

$$\epsilon_{\mathbf{k}\sigma} = \begin{cases} -2t(\cos k_x + \cos k_y) - 2t' \text{sgn}(\sigma)(\cos(k_x + k_y) - \cos(k_x - k_y)), & \text{for } d_{xy} \text{ altermagnetic case,} \\ -2t(\cos k_x + \cos k_y) - 2t' \text{sgn}(\sigma)(\cos 2k_x - \cos 2k_y), & \text{for } d_{x^2-y^2} \text{ altermagnetic case.} \end{cases} \quad (\text{S29})$$

Here, $\hat{\mathbf{s}}_i$ denotes the local spin-density operator for c electrons,

$$\hat{\mathbf{s}}_i = \frac{1}{2} \sum_{\alpha\beta} \hat{c}_{i\alpha}^\dagger \boldsymbol{\sigma}_{\alpha\beta} \hat{c}_{i\beta}. \quad (\text{S30})$$

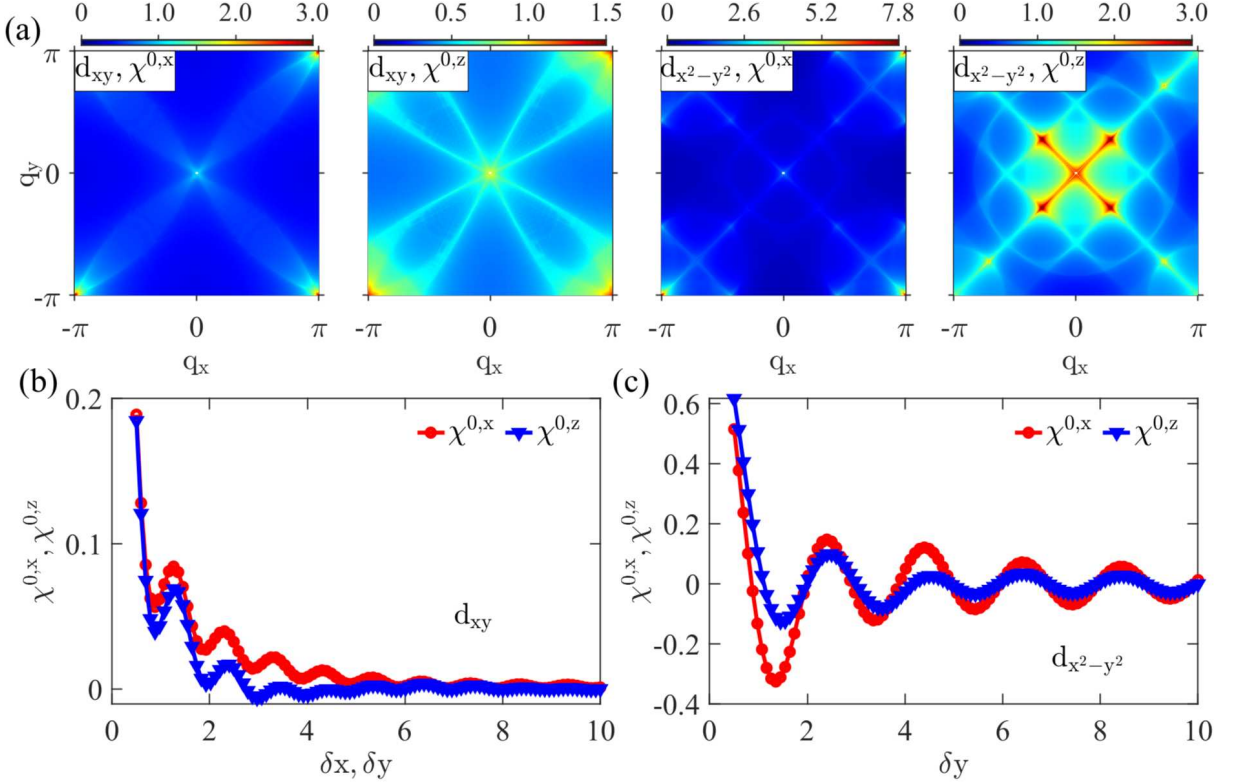


FIG. S2. (a) Momentum dependence of the static spin susceptibilities $\chi^{0,x}$ and $\chi^{0,z}$ for different altermagnetic terms, with $d_{x^2-y^2}$ and d_{xy} indicating the altermagnetic symmetry. Real-space dependence of $\chi^{0,x}$ and $\chi^{0,z}$ along (b) the y direction and (c) the diagonal direction.

By employing the path-integral formalism for spins and fermions and integrating out the fermionic degrees of freedom, the action within second-order perturbation theory can be written as

$$S = S_0(\mathbf{n}) - \frac{J_K^2 s^2}{2} \int_0^\beta d\tau \int_0^\beta d\tau' \sum_{\mu\mu'} n_0^\mu(\tau) C_R^{0,\mu}(\tau - \tau') n_R^\mu(\tau'), \quad (\text{S31})$$

where $\langle n | S_i | n \rangle = s n_i$, and

$$C_R^{0,\mu}(\tau) = \langle T_\tau s_0^\mu(\tau) s_R^\mu(0) \rangle_0. \quad (\text{S32})$$

Here, $S_0(\mathbf{n})$ denotes the non-interacting part of the action. Thus, the RKKY interaction between two local moments separated by distance \mathbf{R} is directly proportional to the non-interacting spin correlation function $C_R^0(\tau)$.

Transforming to momentum space, the spin susceptibility takes the form

$$\chi_{\mathbf{q}}^{0,\mu}(i\omega_n) = - \sum_{\mathbf{k}} \sum_{\alpha\beta} \sigma_{\alpha\beta}^\mu \sigma_{\beta\alpha}^\mu \frac{f(\epsilon_{\mathbf{k}+\mathbf{q},\alpha}) - f(\epsilon_{\mathbf{k},\beta})}{i\omega_n + \epsilon_{\mathbf{k}+\mathbf{q},\alpha} - \epsilon_{\mathbf{k},\beta}}. \quad (\text{S33})$$

In particular, the static spin susceptibility is given by

$$\chi_{\mathbf{q}}^{0,x} = \chi_{\mathbf{q}}^{0,y} = -2 \sum_{\mathbf{k}} \frac{f(\epsilon_{\mathbf{k}+\mathbf{q},\uparrow}) - f(\epsilon_{\mathbf{k},\downarrow})}{\epsilon_{\mathbf{k}+\mathbf{q},\uparrow} - \epsilon_{\mathbf{k},\downarrow}}, \quad (\text{S34})$$

and

$$\chi_{\mathbf{q}}^{0,z} = - \sum_{\mathbf{k}\sigma} \frac{f(\epsilon_{\mathbf{k}+\mathbf{q},\sigma}) - f(\epsilon_{\mathbf{k},\sigma})}{\epsilon_{\mathbf{k}+\mathbf{q},\sigma} - \epsilon_{\mathbf{k},\sigma}}, \quad (\text{S35})$$

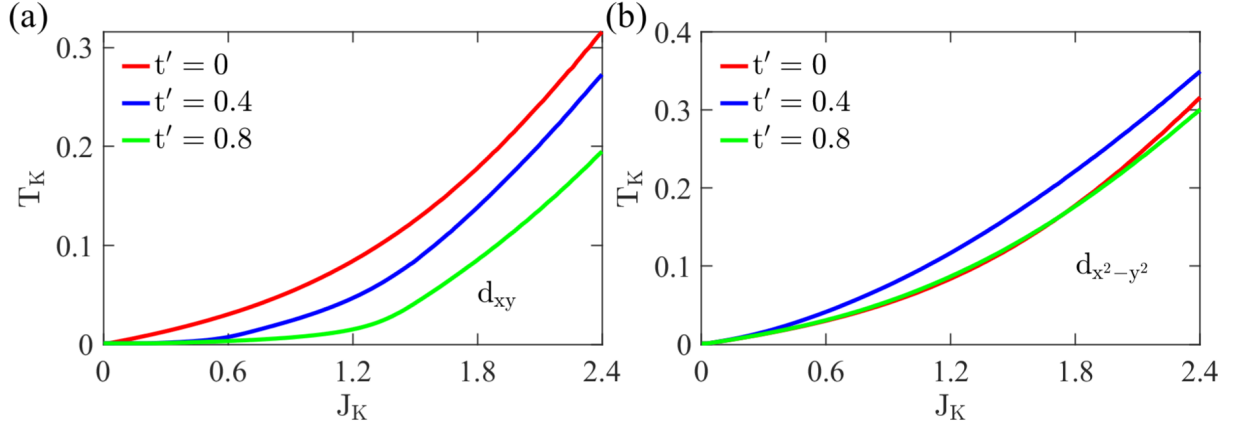


FIG. S3. Mean-field Kondo temperature T_K as a function of the Kondo coupling J_K for different altermagnetic strengths $t' = 0, 0.4, 0.8$, obtained from mean-field calculations for (a) the d_{xy} case and (b) the $d_{x^2-y^2}$ case.

where we omit the zero-frequency label 0.

In the absence of altermagnetic hopping ($t' = 0$), the dispersion satisfies $\xi_{\mathbf{k}\sigma} = \xi_{\mathbf{k}\bar{\sigma}}$ and $\xi_{\mathbf{k}+\mathbf{Q},\sigma} = -\xi_{\mathbf{k}\sigma}$, where $\mathbf{Q} = (\pi, \pi)$. Under these conditions, the spin susceptibilities become isotropic,

$$\chi^{0,x} = \chi^{0,y} = \chi^{0,z}, \quad (\text{S36})$$

and all components diverge at the wavevector $\mathbf{Q} = (\pi, \pi)$, reflecting the perfect nesting of the Fermi surface.

For both the d_{xy} and $d_{x^2-y^2}$ cases, the dispersion satisfies $\xi_{\mathbf{k}+\mathbf{Q},\sigma} = -\xi_{\mathbf{k},\bar{\sigma}}$ with $\mathbf{Q} = (\pi, \pi)$. This nesting condition leads to a divergence in $\chi_{\mathbf{Q}}^{0,x}$, as illustrated in Fig. S2(a). Consequently, $\chi_{\mathbf{Q}}^{0,x} > \chi_{\mathbf{Q}}^{0,z}$, in contrast to the isotropic case where $\chi_{\mathbf{Q}}^{0,x} = \chi_{\mathbf{Q}}^{0,z}$, providing a clear fingerprint of the altermagnetic contributions in the RKKY interaction. In real space, this manifests as oscillations along the y direction, as shown in Fig. S2(c). Along the diagonal direction, although oscillations persist, the values remain predominantly positive, as shown in Fig. S2(b).

If the altermagnetic terms takes the form $-2t' \text{sgn}(\sigma)(\cos k_x - \cos k_y)$, the dispersion satisfies $\xi_{\mathbf{k}+\mathbf{Q},\sigma} = -\xi_{\mathbf{k},\sigma}$, leading to a divergence in $\chi_{\mathbf{Q}}^{0,z}$.

We note that, using Wicks theorem to compute the spin susceptibility of the AM band structure, one can apply the result of the End Matter discussing the symmetry of the Green function, to show that along a nodal line,

$$\chi_{\mathbf{R}}^{0,x}(i\omega_m) = \chi_{\mathbf{R}}^{0,y}(i\omega_m) = \chi_{\mathbf{R}}^z(i\omega_m). \quad (\text{S37})$$

IV. Mean-Field Calculations and Results

For the multi-impurity Kondo model, the mean-field Hamiltonian can be expressed as

$$H_{\text{MF}} = \sum_{\sigma} \hat{\psi}_{\sigma}^{\dagger} h^{\sigma} \hat{\psi}_{\sigma} + \text{const}, \quad (\text{S38})$$

where

$$\hat{\psi}_{\sigma}^{\dagger} = \left(\cdots, \hat{c}_{\mathbf{k}\sigma}^{\dagger}, \cdots, \hat{f}_{1\sigma}^{\dagger}, \cdots, \hat{f}_{n_0\sigma}^{\dagger} \right), \quad h^{\sigma} = \begin{pmatrix} E^{\sigma} & M^{\dagger} \\ M & 0 \end{pmatrix}, \quad E_{ij}^{\sigma} = \epsilon_{\mathbf{k}_i\sigma} \delta_{ij}, \quad M_{ij} = \frac{V_j}{\sqrt{n}} e^{i\mathbf{k}_i \cdot \mathbf{R}_j}. \quad (\text{S39})$$

Here, we have set the Lagrange multiplier to zero. Owing to particle-hole symmetry this sets the average occupancy of the f -electrons to unity.

Within the mean-field approximation, the Hamiltonian can be diagonalized as

$$\hat{\psi}_{\sigma}^{\dagger} h^{\sigma} \hat{\psi}_{\sigma} = \hat{\Gamma}_{\sigma}^{\dagger} \Lambda^{\sigma} \hat{\Gamma}_{\sigma}, \quad \hat{\psi}_{\sigma} = V_{\sigma} \hat{\Gamma}_{\sigma}, \quad V_{\sigma}^{\dagger} h^{\sigma} V_{\sigma} = \Lambda^{\sigma}. \quad (\text{S40})$$

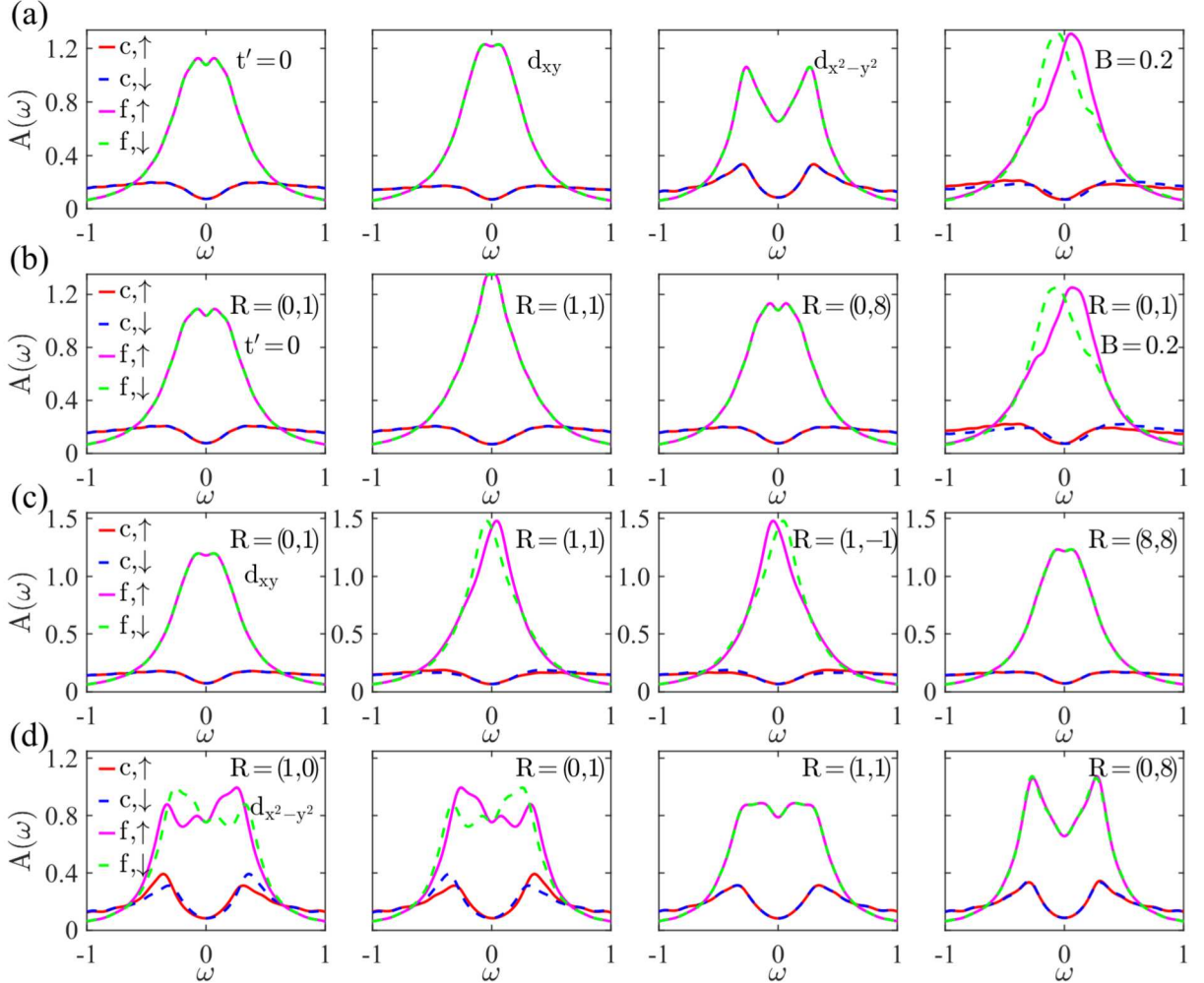


FIG. S4. Spectral functions from the mean-field approximation. (a) Spin-dependent spectral functions of the c and f electrons for the single-impurity Kondo model under different conditions, where d_{xy} and $d_{x^2-y^2}$ indicate the symmetry of the altermagnetism, and $B = 0.2$ denotes the applied magnetic field strength. (b) Spectral functions for the two-impurity Kondo model for various impurity configurations, where \mathbf{R} denotes the distance between the two impurities. (c,d) Spin-dependent spectral functions for the two-impurity Kondo model with d_{xy} and $d_{x^2-y^2}$ altermagnetic terms in the conduction-electron sector, respectively.

The self-consistent hybridization field is determined by

$$\begin{aligned}
 V_l &= -\frac{J_K}{2\sqrt{n}} \sum_{\mathbf{k}\sigma} e^{-i\mathbf{k}\cdot\mathbf{R}_l} \langle \hat{c}_{\mathbf{k}\sigma}^\dagger \hat{f}_\sigma \rangle \\
 &= -\frac{J_K}{2\sqrt{n}} \sum_{\mathbf{k}\sigma} e^{-i\mathbf{k}\cdot\mathbf{R}_l} \sum_j V_{\mathbf{k}j\sigma}^* V_{lj\sigma} f(E_j^\sigma),
 \end{aligned} \tag{S41}$$

where $f(E_j^\sigma)$ is the Fermi-Dirac distribution function.

Within the mean-field framework, the Kondo transition temperature T_K can be determined from the vanishing of the hybridization gap V_l , with the amplitude $|V_l|$ being uniform across different impurity sites. As illustrated in Fig. S3(a) and (b), the Kondo transition temperature increases with the Kondo coupling J_K for various altermagnetic strengths. The approximately linear behavior observed for the $d_{x^2-y^2}$ case may originate from the van Hove singularity at $\mu = 0$ in the corresponding dispersion.

The Green function is defined as

$$G_{l\sigma}^d(\tau) = -\langle T_\tau \left(\hat{d}_{l\sigma}(\tau) \hat{d}_{l\sigma}^\dagger(0) \right) \rangle, \tag{S42}$$

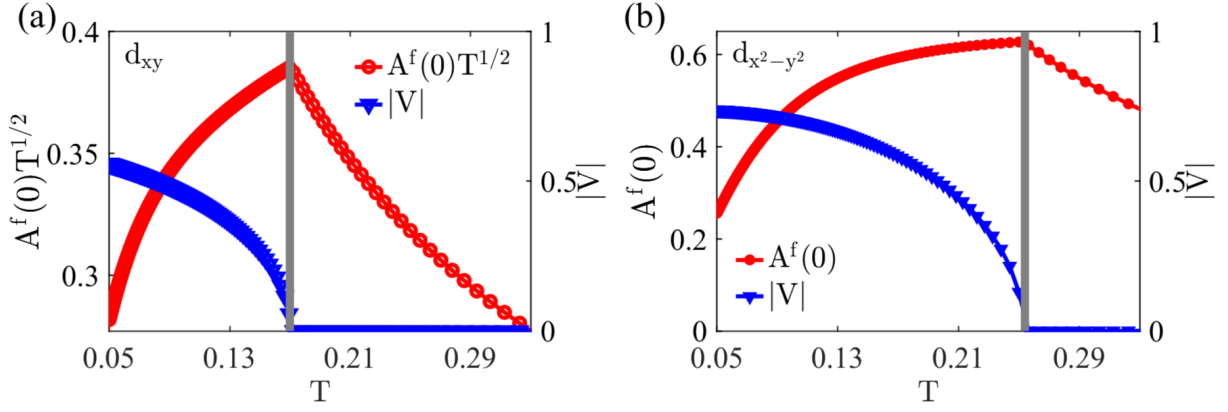


FIG. S5. Temperature dependence of the hybridization gap and the zero-energy density of states $N^f(0)T^{1/2}$ and $N^f(0)$ for the d_{xy} case with $\mathbf{R} = (1, 1)$ and the $d_{x^2-y^2}$ case with $\mathbf{R} = (0, 1)$. Parameters are $J_K = 2$ and $t' = 0.4$.

where $\hat{d}_{l\sigma} = \hat{c}_{l\sigma}$ or $\hat{f}_{l\sigma}$. In the imaginary frequency domain, the Green functions for the conduction and localized electrons are given by

$$G_\sigma^c(\mathbf{k}, i\omega_n) = \sum_j \frac{V_{kj\sigma} V_{kj\sigma}^*}{i\omega_n - \Lambda_j^\sigma}, \quad G_{l\sigma}^f(i\omega_n) = \sum_j \frac{V_{l+N,j\sigma} V_{l+N,j\sigma}^*}{i\omega_n - \Lambda_j^\sigma}. \quad (\text{S43})$$

The corresponding spectral functions can then be expressed as

$$A_\sigma^c(\omega) = \frac{\delta}{\pi} \sum_{\mathbf{k}j} \frac{V_{kj\sigma} V_{kj\sigma}^*}{(\omega - \Lambda_j^\sigma)^2 + \delta^2}, \quad A_{l\sigma}^f(\omega) = \frac{\delta}{\pi} \sum_j \frac{V_{l+N,j\sigma} V_{l+N,j\sigma}^*}{(\omega - \Lambda_j^\sigma)^2 + \delta^2}. \quad (\text{S44})$$

If one adopts a real-space representation for h^σ , it takes the form

$$h^\sigma = \begin{pmatrix} T^\sigma & Q^\dagger \\ Q & 0 \end{pmatrix}, \quad T_{ij} = t_{ij}^\sigma, \quad Q_{ij} = V_j. \quad (\text{S45})$$

The local spectral functions of the c and f electrons are then given by

$$A_{l\sigma}^f(\omega) = \frac{\delta}{\pi} \sum_j \frac{V_{l+N,j\sigma} V_{l+N,j\sigma}^*}{(\omega - \Lambda_j^\sigma)^2 + \delta^2}, \quad A_{l\sigma}^c(\omega) = \frac{\delta}{\pi} \sum_j \frac{V_{lj\sigma} V_{lj\sigma}^*}{(\omega - \Lambda_j^\sigma)^2 + \delta^2}. \quad (\text{S46})$$

As shown in Fig. S4, the spin-dependent spectral functions of the c and f electrons clearly illustrate the effects of the d_{xy} and $d_{x^2-y^2}$ altermagnetic terms. For a single impurity, the altermagnetic terms do not lift the spin degeneracy, whereas an external magnetic field can induce splitting, as illustrated in Fig. S4(a). In the two-impurity case with $t' = 0$, the spectral functions remain spin-degenerate regardless of the impurity separation, while the application of a magnetic field leads to a clear spin splitting, as shown in Fig. S4(b). When the d_{xy} or $d_{x^2-y^2}$ altermagnetic terms are present, the spin splitting of the spectral functions reflects the underlying altermagnetic symmetry, as shown in Fig. S4(c) and (d). At sufficiently large impurity separations, the splitting disappears.

The zero-energy density of states can also be estimated within the mean-field framework using the relation

$$A^f(0) \approx \frac{\beta}{\pi} G(\beta/2). \quad (\text{S47})$$

We observe that, for $\mathbf{R} = (1, 1)$ in the d_{xy} case $A^f(0)T^{1/2}$ exhibits a pronounced peak at the Kondo transition temperature T_K , as shown in Fig. S5, though $A^f(0)$ only has a kink. In contrast, for $\mathbf{R} = (0, 1)$ in the $d_{x^2-y^2}$ case, the transition temperature T_K can be identified by the peak in $A^f(0)$.

V. Symmetry Analysis and Spectral Decomposition

Under the combined operation of time-reversal and particle-hole transformations, the Green function $\tilde{G}_{i\downarrow}(\tau)$ is mapped onto $\tilde{G}_{i\uparrow}(\beta - \tau)$. This relation can be demonstrated explicitly as follows. We start from the definition of the imaginary-time Green function for composite fermion,

$$\tilde{G}_{j\sigma}(\tau) = \langle T_\tau \hat{\psi}_{j\sigma}(\tau) \hat{\psi}_{j\sigma}^\dagger(0) \rangle. \quad (\text{S48})$$

For $\tau > 0$, inserting a complete set of energy eigenstates yields the Lehmann representation [53],

$$\tilde{G}_{j\sigma}(\tau) = \sum_{n,m} e^{-\beta E_n} e^{(E_n - E_m)\tau} \langle n | \hat{\psi}_{j\sigma} | m \rangle \langle m | \hat{\psi}_{j\sigma}^\dagger | n \rangle. \quad (\text{S49})$$

Correspondingly, the associated spectral function can be expressed as

$$\hat{N}_{j\sigma}(\omega) = \sum_{n,m} (e^{-\beta E_n} + e^{-\beta E_m}) \langle n | \hat{\psi}_{j\sigma} | m \rangle \langle m | \hat{\psi}_{j\sigma}^\dagger | n \rangle \delta(\omega + E_n - E_m). \quad (\text{S50})$$

Under the combined operation of time-reversal and particle-hole transformations, the fermionic operator transforms as $\hat{\psi}_{j\downarrow} \rightarrow (-1)^j \hat{\psi}_{j\uparrow}^\dagger$. Accordingly, the matrix elements transform as $\langle n | \hat{\psi}_{j\downarrow} | m \rangle \rightarrow (-1)^j \langle n' | \hat{\psi}_{j\uparrow}^\dagger | m' \rangle$, where $|n'\rangle$ and $|m'\rangle$ denote the transformed many-body eigenstates. As a consequence, the spectral functions satisfy the symmetry relation

$$\tilde{N}_{j\downarrow}(\omega) = \tilde{N}_{j\uparrow}(-\omega). \quad (\text{S51})$$

This symmetry immediately implies a corresponding relation for the imaginary-time Green functions. Using the spectral representation

$$\tilde{G}_{j,\sigma}(\tau) = \int d\omega \frac{\tilde{N}_{j,\sigma}(\omega) e^{-\omega\tau}}{e^{-\beta\omega} + 1}, \quad (\text{S52})$$

we obtain

$$\begin{aligned} \tilde{G}_{j,\uparrow}(\beta - \tau) &= \int d\omega \frac{\tilde{N}_{j,\uparrow}(\omega) e^{-\omega(\beta-\tau)}}{e^{-\beta\omega} + 1} = \int d\omega \frac{\tilde{N}_{j,\uparrow}(\omega) e^{\omega\tau}}{e^{\beta\omega} + 1} \\ &= \int d\omega' \frac{\tilde{N}_{j,\uparrow}(-\omega') e^{-\omega'\tau}}{e^{-\beta\omega'} + 1} = \int d\omega' \frac{\tilde{N}_{j,\downarrow}(\omega') e^{-\omega'\tau}}{e^{-\beta\omega'} + 1} \\ &= \tilde{G}_{j,\downarrow}(\tau), \end{aligned} \quad (\text{S53})$$

which means that $\tilde{G}_{j,\uparrow}(\beta/2) = \tilde{G}_{j,\downarrow}(\beta/2)$.

We then obtain

$$\begin{aligned} \tilde{G}_{j,\uparrow}(\omega = 0) &= \int_0^\beta d\tau \tilde{G}_{j,\uparrow}(\tau) = \int_0^\beta d\tau \tilde{G}_{j,\downarrow}(\beta - \tau) \\ &= \int_0^\beta d\tau' \tilde{G}_{j,\downarrow}(\tau') = \tilde{G}_{j,\downarrow}(\omega = 0). \end{aligned} \quad (\text{S54})$$

Consequently, the imaginary-time integrated Green functions for the two spin components are identical. In particular, the integral of the difference between $\tilde{G}_{R,\uparrow}(\tau)$ and $\tilde{G}_{R,\downarrow}(\tau)$ over imaginary time vanishes,

$$\int_0^\beta d\tau [\tilde{G}_{R,\uparrow}(\tau) - \tilde{G}_{R,\downarrow}(\tau)] = \tilde{G}_{R,\uparrow}(\omega = 0) - \tilde{G}_{R,\downarrow}(\omega = 0) = 0. \quad (\text{S55})$$

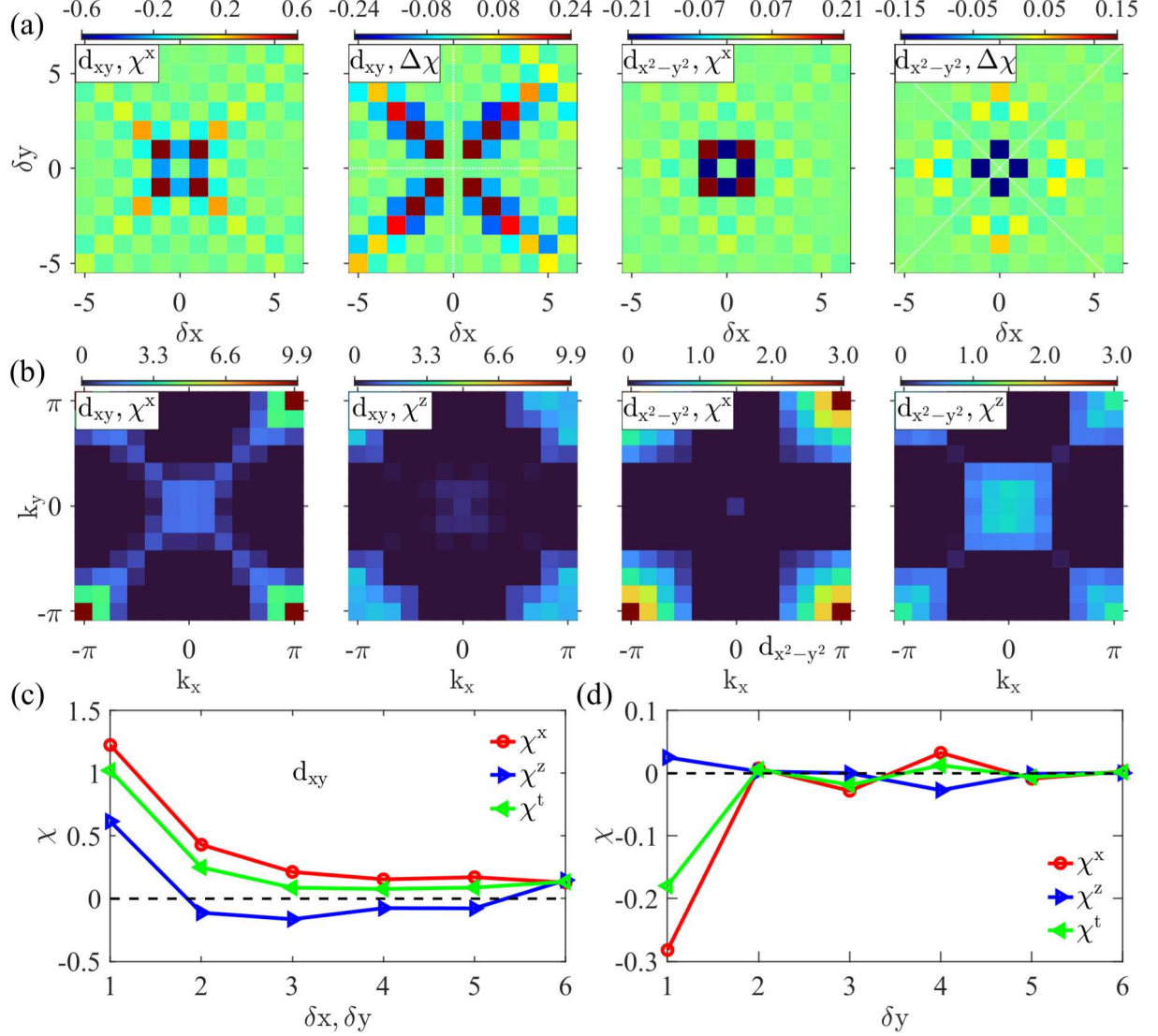


FIG. S6. Spin susceptibility from QMC calculations. (a) Real-space distributions of the x -component static spin susceptibility $\chi_{\mathbf{R}}^x$ and the susceptibility difference $\Delta\chi = \chi_{\mathbf{R}}^x - \chi_{\mathbf{R}}^z$ for the d_{xy} and $d_{x^2-y^2}$ altern magnetic cases at $T = 0.10$. (b) Momentum-space distributions of the x - and z -component static spin susceptibilities, $\chi_{\mathbf{k}}^x$ and $\chi_{\mathbf{k}}^z$, at $T = 0.10$. (c) Distance dependence of the static susceptibilities $\chi_{\mathbf{R}}^x$, $\chi_{\mathbf{R}}^z$, and the total susceptibility $\chi_{\mathbf{R}}^t = (2\chi_{\mathbf{R}}^x + \chi_{\mathbf{R}}^z)/3$ along the diagonal direction for the d_{xy} case at $T = 0.05$. (d) Distance dependence of the static susceptibilities along the y direction for the $d_{x^2-y^2}$ case at $T = 0.05$.

Instead, we introduce the following quantity,

$$\begin{aligned}
 \Delta\tilde{G}_{\mathbf{R}} &= \left(\int_0^{\beta/2} d\tau - \int_{\beta/2}^{\beta} d\tau \right) \left[\tilde{G}_{\mathbf{R},\uparrow}(\tau) - \tilde{G}_{\mathbf{R},\downarrow}(\tau) \right] \\
 &= \left(\int_0^{\beta/2} d\tau - \int_{\beta/2}^{\beta} d\tau \right) \int d\omega \frac{e^{-\omega\tau}}{e^{-\beta\omega} + 1} \left[\tilde{N}_{\mathbf{R},\uparrow}(\omega) - \tilde{N}_{\mathbf{R},\downarrow}(\omega) \right] \\
 &= \int d\omega \frac{1 - e^{\beta\omega/2}}{\omega} \left[\tilde{N}_{\mathbf{R},\uparrow}(\omega) - \tilde{N}_{\mathbf{R},\downarrow}(\omega) \right] f_{\beta}(\omega), \tag{S56}
 \end{aligned}$$

where $f_\beta(\omega) = \frac{1}{\omega} \left(1 - \frac{1}{\cosh(\beta\omega/2)}\right)$ is an odd function of frequency.

Consequently, $\Delta\tilde{G}_{\mathbf{R}}$ vanishes only if the spin-resolved spectral difference $\tilde{N}_{\mathbf{R},\uparrow}(\omega) - \tilde{N}_{\mathbf{R},\downarrow}(\omega)$ contains solely an even-frequency component. In the present case, this difference is purely odd in frequency, leading to a finite $\Delta\tilde{G}_{\mathbf{R}}$.

For the spin correlation function $C(\tau)$, a similar spectral decomposition can be carried out,

$$C(\tau) = \int d\omega \frac{\chi''(\omega) e^{-\omega\tau}}{1 - e^{-\beta\omega}}, \quad (\text{S57})$$

where $\chi''(\omega)$ denotes the imaginary part of the dynamical spin susceptibility.

Accordingly, its imaginary-time integral,

$$\chi(\omega = 0) = \int_0^\beta d\tau C(\tau), \quad (\text{S58})$$

can be analyzed in an analogous manner. The corresponding quantities can be expressed as

$$\chi(\omega = 0) = \int d\omega \frac{\chi''(\omega)}{\omega}, \quad C(\beta/2) = \int d\omega \frac{\chi''(\omega)}{2 \sinh(\beta\omega/2)}, \quad C(0^+) = \int d\omega \frac{\chi''(\omega) e^{-\omega 0^+}}{1 - e^{-\beta\omega}}. \quad (\text{S59})$$

Here, all three quantities are predominantly determined by the low-energy behavior of $\chi''(\omega)$.

In addition, $C(0^+)$ represents an equal-weight superposition of contributions from all imaginary-frequency components. By contrast, $\chi(\omega = 0)$ isolates the zero-frequency (static) component, and therefore more directly reflects the low-energy spin physics of the system.

VI. Static Spin Susceptibility

In addition to the equal-time spin correlations obtained from quantum Monte Carlo simulations, we also analyze the static spin susceptibility, defined as

$$\chi_{\mathbf{R}}^{x(z)} = \int_0^\beta d\tau C_{\mathbf{R}}^{x(z)}(\tau), \quad C_{\mathbf{R}}^{x(z)}(\tau) = \langle T_\tau \hat{S}_{\mathbf{0}}^{x(z)}(\tau) \hat{S}_{\mathbf{R}}^{x(z)} \rangle - \langle \hat{S}_{\mathbf{0}}^{x(z)} \rangle \langle \hat{S}_{\mathbf{R}}^{x(z)} \rangle. \quad (\text{S60})$$

Note that the total spin susceptibility satisfies the relation $\chi_{\mathbf{R}}^t = (2\chi_{\mathbf{R}}^x + \chi_{\mathbf{R}}^z)/3$.

Similar to the equal-time spin correlation, the susceptibility difference $\Delta\chi = \chi_{\mathbf{R}}^x - \chi_{\mathbf{R}}^z$ exhibits nodal lines with the same symmetry: along the x and y directions for the d_{xy} case, and along the diagonal directions for the $d_{x^2-y^2}$ case, as shown in Fig. S6(a). This behavior indicates the restoration of SU(2) spin symmetry along the nodal lines for the corresponding altermagnetic states. In addition, for both cases, the transverse susceptibility $\chi_{\mathbf{R}}^x$ displays a pronounced peak at (π, π) , as shown in Fig. S6(b).

Along the diagonal direction in the d_{xy} case, as shown in Fig. S6(c), $\chi_{\mathbf{R}}^x$ remains positive for all impurity separations, indicating a ferromagnetic interaction between the two impurities along the the diagonal direction. In contrast, $\chi_{\mathbf{R}}^z$ becomes negative at certain distances, signaling the emergence of antiferromagnetic correlations.

Along the y direction in the $d_{x^2-y^2}$ case, both $\chi_{\mathbf{R}}^x$ and $\chi_{\mathbf{R}}^z$ exhibit oscillatory behavior, as shown in Fig. S6(d).

VII. Anisotropic Kondo Screening

We have confirmed that Kondo screening persists even in the presence of altermagnetic terms in the End Matter; however, the screening is anisotropic.

The local spin correlation function $C_l^{x(z)}(\tau)$ is defined as $C_l^{x(z)}(\tau) = \langle T_\tau \hat{S}_{\mathbf{0}}^{x(z)}(\tau) \hat{S}_{\mathbf{0}}^{x(z)} \rangle - \langle \hat{S}_{\mathbf{0}}^{x(z)} \rangle^2$. As shown in Fig. S7(a)(b), $C_l^x(\tau)$ at $T = 0.05$ exhibits noticeable deviations from $C_l^z(\tau)$ at large imaginary times, corresponding to the low-energy regime. In contrast, at low τ , the two correlation functions become nearly identical. This behavior signals anisotropic Kondo screening, with the screening in the z channel being more efficient than that in the x channel.

Such anisotropy can be captured by the anisotropic parameter $\delta(\tau) = [C_l^x(\tau) - C_l^z(\tau)]/[C_l^x(\tau) + C_l^z(\tau)]$, and suggests the emergence of an effective anisotropic Kondo coupling $J_K^{x,z}$ in the low-energy theory, which would naturally appear in a renormalization-group analysis. The magnitude of $\delta(\beta/2)$ in Fig. S7(c)(d) increases upon lowering the temperature, indicating that the anisotropy develops concomitantly with Kondo screening in the presence of antiferromagnetic or ferromagnetic RKKY interactions. As $T \rightarrow 0$, the system approaches the fully Kondo-screened regime, accompanied by a reduction of $\delta(\beta/2)$.

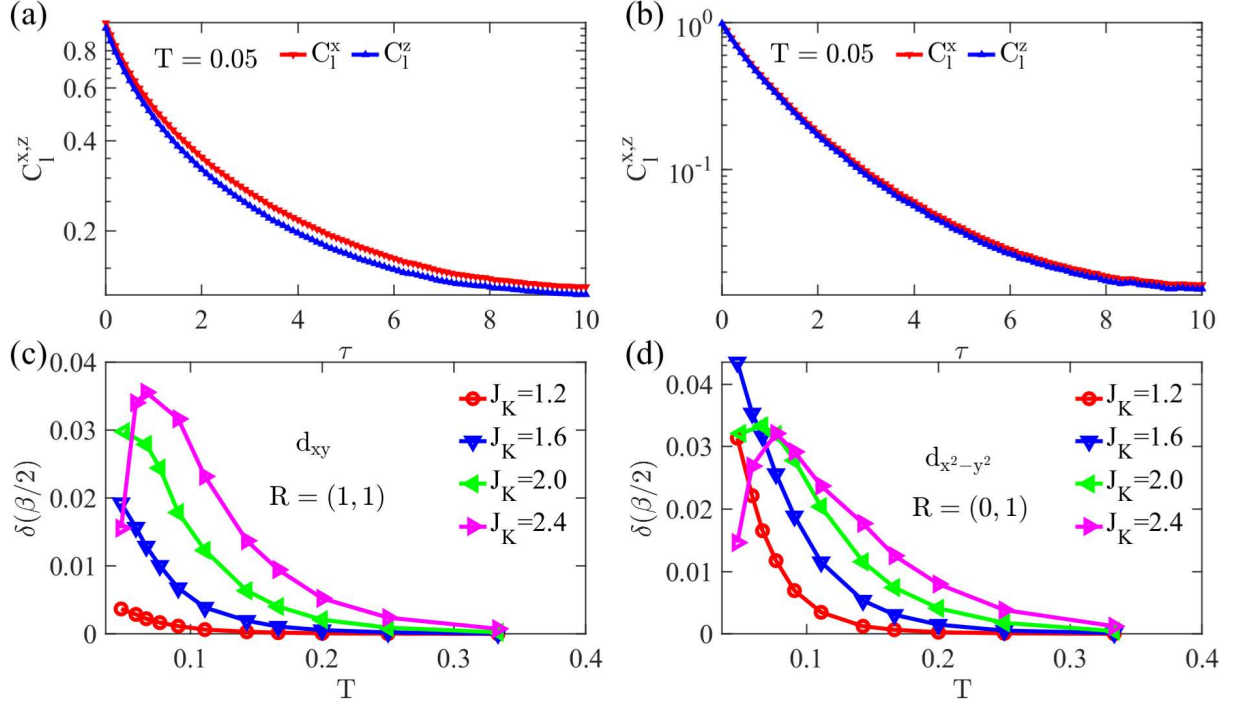


FIG. S7. Anisotropic Kondo Screening for d_{xy} case (a)(c) with $\mathbf{R} = (1, 1)$ and $d_{x^2-y^2}$ case (b)(d) with $\mathbf{R} = (0, 1)$. (a)(b) Local spin correlation functions $C_l^{x(z)}(\tau)$ as functions of imaginary time τ at $T = 0.05$ and $J_K = 2.0$ for d_{xy} and $d_{x^2-y^2}$ symmetry, respectively. (c)(d) Anisotropy of Kondo screening, $\delta(\beta/2) = [C_l^x(\beta/2) - C_l^z(\beta/2)] / [C_l^x(\beta/2) + C_l^z(\beta/2)]$, as a function of temperature at $J_K = 1.2, 1.6, 2.0, 2.4$ for d_{xy} and $d_{x^2-y^2}$ altermagnetic symmetry.